Title: Decoding muscle-resident Schwann cell dynamics during neuromuscular junction remodeling

Authors: Steve D Guzman[1,3], Ahmad Abu-Mahfouz[1], Carol S Davis[1], Lloyd P Ruiz[1], Peter C Macpherson[1], Susan V Brooks[1,2*]

*Corresponding Author: svbrooks@umich.edu

[1]Department of Molecular and Integrative Physiology, University of Michigan, Ann Arbor, MI, USA;
[2]Department of Biomedical Engineering, University of Michigan, Ann Arbor, MI, USA.
[3]Department of Computational Medicine and Bioinformatics, University of Michigan, Ann Arbor, MI, USA.

Abstract

Understanding neuromuscular junction (NMJ) repair mechanisms is essential for addressing degenerative neuromuscular conditions. Here, we focus on the role of muscle-resident Schwann cells in NMJ reinnervation. In young *Sod1*$^{-/-}$ mice, a model of progressive NMJ degeneration, we identified a clear NMJ 'regenerative window' that allowed us to define regulators of reinnervation and crossing *Sod1*$^{-/-}$ mice with *S100GFP*-tg mice permitted visualization and analysis of Schwann cells. High-resolution imaging and single-cell RNA sequencing provide a detailed analysis of Schwann cell number, morphology, and transcriptome revealing multiple subtypes, including a previously unrecognized terminal Schwann cell (tSC) population expressing a synapse promoting signature. We also discovered a novel SPP1-driven cellular interaction between myelin Schwann cells and tSCs and show that it promotes tSC proliferation and reinnervation following nerve injury in wild type mice. Our findings offer important insights into molecular regulators critical in NMJ reinnervation that are mediated through tSCs to maintain NMJ function.

54 **Introduction**

55 The neuromuscular junction (NMJ) is the terminal synapse of the motor system, orchestrating
56 muscle contraction and, by extension, voluntary movement. Effective neurotransmission at the
57 NMJ is paramount for neuromuscular communication, with any degenerative alterations at the
58 synapse having the potential to impair muscle contractile function and overall mobility. NMJ
59 degeneration and denervation are pivotal contributing factors to the onset and progression of
60 degenerative neuromuscular diseases, such as amyotrophic lateral sclerosis (ALS)[1,2], and
61 sarcopenia, the age-related loss of muscle mass and function[3]. The incomplete understanding of
62 mechanisms that control NMJ maintenance and regeneration represents a critical barrier to the
63 development of effective therapeutic interventions for many devastating conditions.

64 The major cellular components of the NMJ are the pre-synaptic motor neuron (MN), the post-
65 synaptic muscle fiber, and supporting glia. The primary glial cell type at the NMJ is a specialized
66 non-myelinating Schwann cell population referred to as terminal Schwann cells (tSCs). tSCs
67 regulate synaptic activity[4], and tSC proliferation is critical to generate a sufficient number of
68 Schwann cells to sustain the physiological regenerative response required for effective muscle
69 reinnervation[5,6]. Despite the importance of SCs and SC proliferation in promoting muscle fiber
70 reinnervation, the cell biology and physiology of muscle resident SCs and their response to
71 denervation remain poorly understood.

72 Widespread and progressive NMJ degeneration and denervation are prominent phenotypes
73 of *Sod1*$^{-/-}$ mice, which lack the enzyme superoxide dismutase 1 (Sod1), making them a broadly
74 used model for testing hypotheses focused on the regulators of NMJ structure and function[7–9].
75 An intriguing recent revelation from this mouse model is a distinct timeframe early in life during
76 which the expression in muscles of acetylcholine receptor alpha (Chrna) mRNA levels and
77 mitochondrial reactive oxygen species (mtROS) production are dramatically but transiently
78 elevated[10]. Upregulation of Chrna and mtROS production are both known to increase significantly
79 in response to muscle denervation[11–13]. The pattern of transient increases around 2 months of

80 age and return to baseline by 3 months for both Chrna mRNA and mtROS suggests a robust
81 denervation/reinnervation event that identifies a potential 'regenerative window' in which the
82 regulation of NMJ repair processes can be examined in detail.

83 To comprehensively assess the role of muscle-resident Schwann cells in these processes,
84 we crossed *Sod1*$^{-/-}$ mice with *S100GFP*-tg mice[14] that express green fluorescent protein driven
85 by the S100B promoter, to create *S100GFP*-tg *Sod1*$^{-/-}$ mice, in which Schwann cells could be
86 easily visualized and subsequently isolated for detailed molecular analysis. Using these mice, we
87 assessed functional innervation, evaluated morphological features of tSCs in conjunction with
88 pre- and post-synaptic structural attributes of NMJs, and performed single-cell RNA-sequencing
89 on muscle-resident Schwann cells during the putative regenerative window between 1 and 3
90 months of age. We validated the occurrence and time course of an extensive denervation event
91 followed by a successful reinnervation response that involves substantial tSC proliferation. Our
92 muscle Schwann cell sequencing data provides single-cell resolution unprecedented in existing
93 data sets, elucidating several muscle-resident Schwann cell subtypes, including the emergence
94 of a previously unreported tSC subtype associated with the denervation-reinnervation response
95 marked by a neurogenic transcriptomic signature. Finally, we reveal a novel cell-cell interaction
96 driven by SPP1 signaling between myelin-producing Schwann cells and tSCs and provide
97 evidence that this interaction promotes proliferation of tSCs at the NMJ following acute nerve
98 injury and is critical for successful reinnervation. Collectively, this work provides important new
99 insights into the biology of muscle-resident glial cells that may be exploited for new therapeutic
100 interventions for neurodegenerative and denervating disorders.

101

102 **Results**

103 ***Sod1*$^{-/-}$ mice display dramatic denervation and reinnervation between 1 and 3 months of**
104 **age.** To directly validate prior findings that suggest an early-life transient NMJ denervation and
105 regenerative event in *Sod1*$^{-/-}$ mice[10], we performed functional, molecular, and morphological

106 assessments of NMJ integrity on *S100GFP*-tg S*od1*$^{-/-}$ mice between 1 and 3 months of age. We
107 first measured gastrocnemius (GTN) muscle contractile properties in situ in anesthetized mice
108 using both nerve stimulation and direct muscle stimulation (Fig. 1a). Comparing these two
109 measurements provides an indication of the level of functional NMJ neurotransmission[15]. As
110 indicated by the representative experimental records in Figure 1b, forces developed by muscles
111 of 2-month-old *S100GFP*-tg S*od1*$^{-/-}$ mice during nerve stimulation were approximately 33% lower
112 than controls, whereas the forces generated in response to direct muscle stimulation were not
113 significantly different between the genotypes (Fig. 1b). Thus, when comparing forces developed
114 during nerve stimulation to those developed during direct muscle stimulation, a deficit of 25% was
115 observed for 2-month-old *S100GFP*-tg S*od1*$^{-/-}$ mice compared with controls (Fig. 1c) indicating
116 the presence of a population of fibers that were not activated in response to nerve stimulation at
117 this age. In contrast to the deficit observed at 2 months for *S100GFP*-tg S*od1*$^{-/-}$ mice, the nerve-
118 to-muscle stimulation force ratio for *S100GFP*-tg mice remained consistent at approximate 1.0
119 across all ages consistent with a high degree of fidelity in functional neurotransmission in control
120 mice across all NMJs during this time window (Fig. 1c). The impairments in neurotransmission in
121 *S100GFP*-tg S*od1*$^{-/-}$ mice were observed only at 2 months, as indicated by no significant
122 difference in the forces elicited by nerve and direct muscle stimulation at 1 month or 3 months
123 (Fig 1c).

124 To investigate the activation of denervation response pathways in *S100GFP*-tg S*od1*$^{-/-}$
125 mice, we analyzed whole muscles by RT-qPCR and demonstrated increased mRNA levels
126 compared to controls for putative genes involved in neuromuscular denervation, Schwann cell
127 activation, and axonal growth (Fig. 1d). These included genes associated with post-synaptic
128 organization (Chrna1, Agrn)[16,17], Schwann cell repair and trophic support (Ngfr, Gdnf)[18,19], cell
129 proliferation (Mki67, Ccnd1)[20–22], Schwann cell development (Sox10)[23], synapse elimination
130 (Cd68)[24,25], and pre-synaptic axonal projection (Gap43, Ntn1)[26,27]. Transcriptional activation of
131 denervation responsive genes and genes indicative of Schwann cell activation was observed in

132 both GTN and tibialis anterior (TA) muscles in *S100GFP*-tg S*od1*$^{-/-}$ mice. Together, our functional
133 data and qPCR data show that between 1 and 3 months of age *S100GFP*-tg S*od1*$^{-/-}$ mice
134 experience transient but recoverable functional neuromuscular alterations with upregulation of
135 molecular pathways known to be associated with NMJ remodeling. We next aimed to directly
136 assess the integrity of the NMJs morphologically and define the cellular response of the tSCs.
137
138 **The remodeling of neuromuscular junctions is associated with increased numbers of tSCs**
139 **and larger synaptic areas.** In addition to the functional and molecular assessments described
140 above, we directly assessed the cellular and morphological response during the denervation-
141 reinnervation event exhibited by *Sod1*$^{-/-}$ mice. We performed detailed imaging of fixed fiber
142 bundles derived from *S100GFP*-tg S*od1*$^{-/-}$ and *S100GFP*-tg controls at 1, 2, and 3 months of age.
143 Our comprehensive analysis covered NMJ structure, accounting for 16 distinct features related to
144 pre- and post-synaptic structures as well as tSC number and morphology (Fig. 2a,b). Detailed
145 descriptions of each morphological feature and how it was derived are described in Extended
146 Data Fig 1. Our findings revealed generalized decreases in *S100GFP*-tg *Sod1*$^{-/-}$ mice compared
147 to controls in the nerve terminal perimeter and the overlap of the nerve terminal with AChRs by
148 33% and 60% respectively (Fig. 2c). Meanwhile, the area of AChRs was observed to be 30%
149 larger in S100GFP-tg *Sod1*$^{-/-}$ mice compared to controls. In addition, the total tSC area and count
150 per NMJ were 60% and 3-fold greater, respectively, in the *S100GFP*-tg *Sod1*$^{-/-}$ group compared
151 to controls (Fig. 2d). As a result of the large increase in tSC number, the area per tSC was 38%
152 smaller in *S100GFP*-tg *Sod1*$^{-/-}$ mice, suggesting a reduced tSC domain at the NMJ. Given that
153 both central and peripheral glia respond to neuronal injury by increasing cell number[5,28], increased
154 tSC number and area at the NMJ are likely acting to protect or promote NMJ integrity during the
155 early neuromuscular events linked to the *Sod1*$^{-/-}$ phenotype.
156 Both the degree of overlap and the size of the synaptic area serve as indicators of how
157 well the pre- and post-synaptic components are in physical congruence[29]. These markers are

158 robust histological indicators of nerve-to-muscle connections. The percentage of overlap between
159 the nerve terminal and AChR was decreased at 2 months but returned to control levels by 3
160 months in *S100GFP*-tg *Sod1*$^{-/-}$ mice (Fig 2e). Re-establishment of control levels of overlap could
161 be explained primarily by presynaptic responses, compensatory postsynaptic changes, or a
162 combination. Our analysis revealed an expansion in synaptic area in between 2 and 3 months in
163 *S100*GFP-tg *Sod1*$^{-/-}$ mice driven largely by an enlargement in nerve terminal area at the age of 3
164 months (Extended Data Fig 1c). The restoration in the degree of overlap coupled with the
165 reduction in denervated NMJs (characterized by NMJs with less than 10% overlap) (Fig. 2e)
166 observed at 3 months collectively indicate muscle reinnervation.

167 In addition to considering specific features associated with NMJ structure individually, we
168 also successfully distilled the 16 features of NMJ morphology measured into an overall
169 assessment of the state of the NMJs through unbiased clustering using uniform manifold
170 approximation and projection (UMAP) (Fig 2f) and k-means clustering (Fig 2g). This analysis
171 resulted in four distinct NMJ clusters (Fig 2g). Clusters 1, 2 and 3 were predominantly composed
172 of WT animals (all ages) and 1-month old *Sod1*$^{-/-}$ mice. Cluster 4, on the other hand, was only
173 composed of NMJs from *Sod1*$^{-/-}$ mice, with nearly 76% of the NMJs in 2-month-old mice appearing
174 in cluster 4. Consistent with the findings described above indicative of NMJ regeneration and
175 reinnervation by 3 months in *Sod1*$^{-/-}$ mice, the majority of NMJs at this age appeared in one of the
176 "clusters associated with WT "innervated" NMJs; however, about 46% of the NMJs retained
177 features that placed them in cluster 4 (Fig 2g). The radar plots and representative images depicted
178 in Fig. 2h,i illustrate the distinctive NMJ feature compositions within each cluster. Clusters 1
179 through 3 exhibited a high degree of overlap, with each subsequent cluster containing
180 progressively larger NMJs. Cluster 4 is distinctive, presenting NMJs exhibiting higher numbers of
181 tSCs, smaller nerve terminal dimensions, larger post-synaptic proportions, prevalent poly-
182 innervation, and axonal blebbing. These results illuminate the heterogeneity and dynamic nature

183 of NMJ morphology as well as the spectrum of structural modifications observable during NMJ
184 remodeling in muscles experiencing partial denervation.

185 Based on our findings that NMJs in 2-month-old *Sod1*$^{-/-}$ mice were characterized by higher
186 numbers of tSCs than observed in other groups, we aimed to verify the presence of proliferation
187 of *S100*GFP+ cells at the NMJs in these mice. To directly test this, we stained muscle bundles
188 with an anti-Ki67 antibody (Fig. 3). We found large numbers of Ki67+ nuclei in the fiber bundles
189 from *Sod1*$^{-/-}$ mice compared to age matched WT mice. Moreover, the majority of Ki67+ nuclei
190 originated from cells that were also *S100*GFP+ positive. Ki67+ cells were observed both in
191 perisynaptic and extrasynaptic locations (within 50 microns of the nearest NMJ). These
192 observations corroborate our earlier finding of a 3-fold increase in tSCs, in *Sod1*$^{-/-}$ mice at two
193 months of age when compared to wild-type controls (Fig. 2c).

194 Collectively, our functional and morphological data strongly support the existence of a key
195 regenerative window centered around 2 months of age in *Sod1*$^{-/-}$mice that is ideal for studying the
196 cellular and molecular changes in muscle Schwann cells during NMJ remodeling and
197 reinnervation. We also present compelling evidence that this remodeling process includes, at
198 least in part, the growth of Schwann cells located in the muscle at the NMJ and a promotion of
199 increased synaptic area through nerve terminal growth. Thus, we next aimed to define the
200 transcriptional response of muscle-resident Schwann cells during NMJ remodeling.

201

202 **scRNA-Seq reveals a unique muscle-resident Schwann cell subtype.** While the classification
203 of Schwann cells has largely relied on histological examination and scRNA-Seq from nerve
204 extracts[30], transcriptomic data on muscle-resident Schwann cells, especially tSCs, remain
205 scant[31,32]. A particular challenge faced by these studies is the rarity of tSCs and the extensive
206 tissue requirement, limiting the cell numbers previously analyzed to as few as 100 individual cells.
207 To overcome this limitation and gain a thorough understanding of the transcriptomic changes in
208 muscle-resident Schwann cells, as well as other cells in the muscle microenvironment during NMJ

209 remodeling, we used scRNA-Seq on pooled TA and GTN muscles from both *S100GFP*-tg and
210 *S100GFP*-tg *Sod1*$^{-/-}$ mice at 2 months of age (Fig 4a). After digesting the muscles, we sorted
211 GFP+ PI- and GFP- PI- single cells using fluorescence-activated cell sorting (FACS) and then
212 subjected the cells to droplet-based scRNA-Seq. Post sequencing and quality control, we
213 successfully isolated a rich population of both GFP+ and GFP- cells (Fig. 4b). Our unbiased
214 clustering approach using uniform manifold approximation and projection (UMAP) classified
215 15,256 cells [*S100GFP*-tg (n =5,260); *S100GFP*-tg *Sod1*$^{-/-}$ (n = 9,996)] into 11 non-Schwann cell
216 clusters and 4 Schwann cell clusters including 2 myelin Schwann cell clusters and 2 terminal
217 Schwann cell (tSC) clusters (Fig 4c). All the identified Schwann cell clusters displayed classic SC
218 markers such as *S100b* and *Sox10*. Notably, clusters of myelin Schwann cells were marked by
219 the expression of myelin-associated genes like *Mbp* and *Mpz* (Fig. 4d), while tSC clusters
220 presented the expression of recently reported non-myelin SC markers, *Ng2* and *Kir4.1* (Fig.
221 4d)[31,33]. Additionally, tSC clusters prominently expressed the essential NMJ organizing gene,
222 Agrn[34], the neurotrophic receptor gene, nerve growth factor receptor (Ngfr), and cyclin-D1
223 (Ccnd1) a recognized gene associated with Schwann cell proliferation (Fig. 4d)[22]. Both *S100GFP*-
224 tg and *S100GFP*-tg *Sod1*$^{-/-}$ samples displayed a comparable total number of Schwann cells (1,739
225 and 1,673, respectively).

226 Our data indicates the presence of at least two distinct tSC subgroups, which we termed
227 tSC-A and tSC-B. Remarkably, we observed 8.5-fold greater representation of the tSC-B
228 subgroup in *S100GFP*-tg *Sod1*$^{-/-}$ mice than in *S100GFP*-tg control mice accounting for 35.9% of
229 the total SC population in *Sod1*$^{-/-}$ mice compared with just 4.3% for control mice (Fig. 4e). In
230 addition, the *S100GFP*-tg *Sod1*$^{-/-}$samples showed a lower percentage of myelin SCs (47.8%)
231 when compared to the 78.8% in the control group. Both tSC clusters prominently displayed the
232 previously identified tSC marker, Cd44[35], as well as the synaptic adhesion molecule, Cadm1. One
233 significant observation was the robust expression in tSCs of Sox6, which is crucial for
234 neurogenesis[36] and prevents early cell cycle exit in glial oligodendrocyte precursor cells[37] but is

235 absent in adult mouse mSCs[38]. Within the tSC-B subgroup, we identified specific expression of
236 genes such as Pde10a, which is notably prevalent in the CNS[39], as well as Runx2 and Tnc, which
237 were specific to tSC-B (Fig. 4f) and have both recently been found at elevated levels in muscle-
238 resident Schwann cells in Sod1G93A mice and in acutely denervated mouse muscles[32].

239 Pathway analysis revealed that genes upregulated in the tSC-B cluster, compared to the
240 other muscle-resident Schwann cell types, were primarily involved in processes like synapse
241 organization (*Gap43, Tnc, Sema3e, Negr1, Cadm1, Ntng1*), neuron projection extension (*Postn,*
242 *Plxna4, Sema3e*), neuron migration (Adgrl3, Chl1, Ptpzr1) and extracellular matrix organizing
243 processes (*Adamtsl1*, *Col27a1*, *Col5a2*, *Lgals3*) (Fig. 4g, Extended Data Fig. 3). The tSC-B
244 cluster also showed downregulated biological processes involved in myelination, myelin assembly
245 and Schwann cell differentiation (Fig. 4h). Overall, our findings delineate two distinct tSC
246 subtypes, tSC-A and tSC-B, with the latter manifesting an enrichment in 2-month-old *Sod1*$^{-/-}$ mice
247 and presenting a transcriptomic signature linked to cell adhesion, synapse organization, and axon
248 regeneration. Based on these findings, we hypothesize that tSC-B is a critical sub-population of
249 tSCs for successful NMJ reinnervation.

250

251 **Intercellular communication network analysis reveals a novel Spp1 signaling dynamic**
252 **between myelin SCs and terminal SCs.** To elucidate the interactions between muscle-resident
253 Schwann cells and other cells within the skeletal muscle niche during the robust NMJ remodeling
254 event identified in young *Sod1*$^{-/-}$ mice, we performed an intercellular communication network
255 analysis on a subset of cells from our scRNA-Seq dataset using CellChat[40]. Information flow for
256 secreted signaling pathways was performed to identify signaling pathways that are changed in
257 *S100GFP*-tg *Sod1*$^{-/-}$ muscles relative to control. We observed that Growth Arrest Specific (GAS)
258 signaling, a crucial regulator of proliferation inhibition, was predominantly expressed in myelin
259 SCs of *S100GFP*-tg compared to *S100GFP*-tg *Sod1*$^{-/-}$ mice (Fig. 5a, Extended Fig. 4b). GAS
260 incoming signaling pattern was found to be low in the proliferating cell and tSC-B cell clusters

261 (Extended Fig. 4a). Interestingly, the PERIOSTIN and SPP1 signaling network displayed an
262 information flow magnitude that was amplified by 40-fold in the *S100GFP*-tg *Sod1*$^{-/-}$ group relative
263 to the *S100GFP*-tg group (Fig 5a). Both periostin and Spp1 signaling have been implicated in
264 promoting tumor cell growth and are also known to be upregulated following nerve injury.

265 Our finding of marked induction of Spp1 signaling in *S100GFP*-tg *Sod1*$^{-/-}$ mice is
266 compelling in light of a recent study finding that Spp1 promotes Schwann cell proliferation and
267 survival, and its expression is notably upregulated in myelin Schwann cells following human
268 peripheral nerve injury[41]. Exploring Spp1 signaling in our dataset, we identified a predominant
269 expression of Spp1 in myelin SCs (Fig. 5b,c). While SPP1 appears to communicate with almost
270 every cell type, a marked increase in inferred SPP1 signaling was observed in *Sod1*$^{-/-}$ mice (Fig
271 5c). Moreover, heightened incoming signals were predicted in tSC-B cells, alongside other cells,
272 including mesenchymal stem cells and proliferative cells (Fig. 5c, Extended Data Fig. 4b).
273 Notably, a significant communication probability was observed between myelin Schwann cells,
274 mainly mSC-A, and tSCs in *Sod1*$^{-/-}$ mice, facilitated through the Spp1-Cd44 and Spp1-(Itgav-
275 Itgab1) signaling (Fig 5d).

276 To validate our CellChat findings, we performed targeted RT-qPCR to evaluate the
277 expression levels of key genes within the Spp1 pathway in GTN muscles isolated from 2-month-
278 old *S100GFP*-tg and *S100GFP*-tg *Sod1*$^{-/-}$ mice (Fig. 5e). We showed upregulation in the
279 expression of Tgfb1, Tgfbr2, and Spp1 in *Sod1*$^{-/-}$ mice. While Cd44 levels remained unchanged,
280 we detected a borderline significant elevation in Cd44v6 ($p = 0.052$), the specific receptor variant
281 of Cd44 known to bind Spp1. We next sought to confirm our scRNA-Seq and bioinformatic findings
282 by pinpointing the protein localization of Spp1 in muscle fibers. Histological analysis using an
283 Spp1 antibody on fixed muscle fiber bundles revealed pronounced localization of Spp1 in myelin
284 SCs near the NMJ, with intensified staining observed in *Sod1*$^{-/-}$ mice (Fig. 5g) compared to control
285 (Fig. 5f). In addition, we validated the protein localization of CD44 in tSCs (Extended Data Fig.
286 4c). Taken together, our findings illuminate a novel Spp1 signaling mechanism involving both

287 myelin SCs and tSCs, which could play a role in enhancing the tSC proliferation and survival
288 during muscle denervation important for successful NMJ remodeling and reinnervation.
289
290 **Spp1 gene expression is markedly increased in muscles following nerve injury.** To explore
291 whether an acute recoverable nerve injury alters the gene expression dynamics of Spp1 signaling
292 in skeletal muscle, we performed sciatic nerve crush procedures on 2-month-old C57BL/6 mice
293 (Fig. 6a). Subsequently, we assessed transcript levels of denervation response pathways and
294 genes involved in SPP1 signaling in GTN muscles in naïve non-injured controls, and 7-, 14-, and
295 28-days post injury (DPI). We observed a striking elevation in Spp1 expression, and its receptors
296 Cd44 and Itgav, peaking at 7 DPI and subsequently reverting to baseline levels by 14 DPI (Fig
297 6b). This temporal trend closely parallels the known post nerve injury gene expression pattern of
298 Chrna1[13], suggesting an inverse relationship with muscle innervation. In addition, Tgfb1 and its
299 receptor Tgfbr2, proposed to be upstream of Spp1 signaling were also elevated at 7 DPI, with
300 Tgfbr2 expression being reduced at 28 DPI compared to uninjured controls. Gene expression for
301 NGFR and GDNF, which are associated with Schwann cell mediated nerve regeneration, were
302 also highly expressed at 7 DPI, while the cell proliferation gene, Ccnd1, was elevated at 7 DPI
303 and persisted at high levels out to 14 DPI. Protein localization of Spp1 was also validated using
304 immunofluorescent imaging of muscle fiber bundles, which showed Spp1 localized to myelin
305 Schwann cells, as well as other GFP+ cells and GFP- cells (Extended Data Fig. 5). The
306 pronounced Spp1 expression during the initial nerve regeneration phase and its subsequent
307 normalization is consistent with known muscle reinnervation milestones and implicates the
308 potential involvement of Spp1 in muscle reinnervation.
309
310 **Inhibition of muscle Spp1 after acute nerve injury results in reduced muscle reinnervation**
311 **and fewer tSCs.** To determine the role of Spp1 signaling in muscle reinnervation and its potential
312 mediation of tSC responses post-nerve injury, we carried out peroneal nerve crush injuries on

313 control *S100GFP*-tg mice and administered intramuscular injections of either an Spp1 neutralizing
314 antibody (Spp1-nAb) or saline (Fig 6c). Evaluations of recovery of functional neurotransmission
315 as assessed by the ability of nerve stimulation to activate muscle contractions and tSC
316 characteristics were conducted at 7 DPI. To expedite the evaluation of the onset of muscle
317 reinnervation and reduce the number of muscle injections, nerve injuries were strategically
318 performed near the nerve entry point of the TA muscle, with muscles receiving injections at the
319 time of injury and every two days thereafter. Evoked force measurements by direct muscle
320 stimulation showed no difference between the saline- and Spp1-nAb-treated groups; however,
321 nerve evoked muscle forces were 43% lower for muscles of mice treated with Spp1-nAb (Fig 6d).
322 Furthermore, nerve-to-muscle force ratios in Spp1-nAb administered mice were 38% lower than
323 for muscles of saline-treated mice. Collectively, these findings suggest that functional
324 reinnervation post-injury was either impaired or delayed by neutralizing intramuscular Spp1
325 signaling.

326 We concurrently evaluated the effects of intramuscular Spp1 neutralization on tSCs in
327 fixed muscle fiber bundles following injury histologically (Fig. 6e). Mice treated with Spp1-nAb at
328 7 DPI displayed a pronounced decrease in the nerve terminal area, perimeter, and synaptic area
329 in comparison to the saline-treated controls (Fig 6f). In terms of denervated NMJs, the Spp1-nAb-
330 treated group exhibited a significantly higher proportion of denervated muscle fibers relative to
331 the saline-treated group (67% Spp1-nAb vs 33% saline), and NMJ synaptic area was also lower
332 in Spp1-nAb mice. Further examination of tSC characteristics revealed a diminished number of
333 tSCs per NMJ and a smaller tSC area for muscles that had Spp1 signaling inhibited (Fig 6f).
334 Taken together, this evidence, coupled with our functional analyses, underscores the role of Spp1
335 in muscle reinnervation and its involvement in augmenting the tSC count at the NMJ.

336

337 **Discussion**

338 To our knowledge, the current study boasts the most detailed scRNA-Seq repository to
339 date of muscle-resident Schwann cells, encompassing tSCs, across both healthy and partially
340 denervated muscles. The results presented elucidate the critical role of a previously unrecognized
341 reactive population of tSCs that has synapse promoting, cell adhesion, and ECM organizing
342 properties. One prior study isolated tSCs using a dual mouse reporter that expressed both NG2-
343 dsRed and S100GFP and performed bulk-RNA Seq[31], but bulk sequencing doesn't allow for the
344 distinction between different tSC subtypes or illuminate cell specific responses to NMJ
345 remodeling. Our data also demonstrate that this reactive phenotype is underpinned by an intricate
346 SPP1 signaling mechanism, bridging myelin Schwann cells and tSCs. Our observations of
347 marked elevations in both Spp1 gene expression and protein immunofluorescence in the acute
348 phase post muscle denervation is consistent with prior reports of induction of Spp1 in samples
349 from nerve injury patients[41], and we show for the first time that Spp1 expression has functional
350 relevance for the efficacy and/or efficiency of the response of tSCs to effect NMJ reinnervation.
351 This significant conclusion is supported by our observations of increased tSC numbers following
352 peroneal nerve injury that were notably decreased following intramuscular administration of an
353 Spp1-nAb resulting in a diminished synaptic contact area, a pronounced percentage of
354 denervated NMJs, and impaired recovery of functional innervation. Collectively, our findings
355 suggest a pivotal role of Spp1 signaling, facilitated by myelin Schwann cells, in regulating tSC
356 proliferation and reinnervation of denervated NMJs.

357 While upregulation of Spp1 in muscles of patients suffering from Duchenne Muscular
358 Dystrophy (DMD)[42] and in mice following exercise[43] has been reported, our study uncovers a
359 novel cellular origin contributing to this signaling — originating from muscle-resident myelin
360 Schwann cells, rather than or perhaps in addition to macrophages targeting Fibro/adipogenic
361 progenitors (FAPs)[43–45]. The strong induction of Spp1 signaling pathway transcripts we observed
362 concurrent with intense Spp1 immunofluorescence in skeletal muscle after nerve injury suggests
363 Spp1 may have multiple functions to mediate muscle reinnervation. Integral to muscle

364 reinnervation is Wallerian degeneration, a process governed by dynamic interactions among
365 immune cells, FAPs, and Schwann cells. Thus, it is reasonable to hypothesize that Spp1 engages
366 with multiple cell types in response to severe nerve trauma, such as nerve crush or nerve
367 transection, to facilitate myelin clearance, ECM remodeling, and axon regeneration. In contrast,
368 our observations, based on both imaging for protein and scRNA-Seq, of no significant Spp1
369 signaling stemming from immune cells in muscles of *Sod1*$^{-/-}$ mice disrupts conventional
370 understanding of Spp1 signaling in muscle. These findings open the door for additional studies of
371 the necessity for engaging immune cells during transient physiological innervation remodeling.
372 Spp1 signaling between glial cell subtypes is further supported by recent investigations showing
373 elevated levels of Spp1 in nerve samples post-injury, which positively correlated with Schwann
374 cell proliferation and survival[41]. Furthermore, Spp1 has neuroprotective roles in the eye and is
375 expressed by reactive astrocytes to promote retinal ganglion cell survival after traumatic optic
376 nerve damage[46]. Beyond this regenerative aspect, Spp1 is implicated in pathological contexts,
377 including tumor growth and metastasis, highlighting its versatility and likely the complexity of its
378 regulation in promoting cell survival and growth in various contexts and cell types.

379 The synaptic regenerative signature we identified in tSCs during their response to
380 denervation is distinctly characterized by the expression of *Gap43* and *Ntng1*. Gap43 is noted for
381 its concentrated presence within regenerating growth cones of neurons and plays an
382 indispensable role in axon guidance[47]. The expression of Gap43 is not exclusive to neurons but
383 is also found in reactive astrocytes and in tSCs after denervation, correlating with the elongation
384 of tSC processes[48,49]. Beyond axonal guidance, Gap43 is also involved in the transfer of
385 mitochondria between astrocytes and glioblastoma cells[50]. Given that mitochondria are abundant
386 within growth cones to meet energy demands[51], one might speculate that Gap43+ tSCs promote
387 axon regeneration through mitochondrial transfer, thereby contributing to metabolic support. This
388 proposition opens new areas for exploring unconventional pathways of axon regeneration and
389 delineating the multifaceted roles of Gap43 in neural repair mechanisms. Netrins are also

390 important for axon guidance and has been shown to promote SC migration and proliferation[52,53].
391 Recently, Ntng1 was discerned to facilitate signaling interactions between tSCs and sensory
392 neurons, crucial for organogenesis in both hairy and non-hairy skin[54]. The expression of *Ntn1g* in
393 muscle-resident tSCs could function to support reinnervation of the endplate after denervation.
394 Collectively, the expression of synaptic related genes in tSCs highlights the potential for new
395 therapeutic targets to promote NMJ repair.

396 Cellular proliferation is universally recognized as a fundamental mechanism in various
397 tissue regeneration processes. The proliferation dynamics of myelin Schwann cells have been
398 extensively studied, with nerve injuries recognized as their primary trigger. A pertinent example
399 is the marked 3 to 4-fold elevation in Schwann cell numbers observed within a week of sciatic
400 nerve injury[55]. Although inhibition of Cyclin D1 mediated Schwann cell proliferation was ineffective
401 in preventing nerve regeneration in the distal sciatic nerve stump[56], that study did not examine
402 muscle-resident Schwann cells nor perform any functional assessment of NMJ transmission. tSCs
403 not only proliferate after nerve injury but also extend cytoplasmic processes, promoting axonal
404 sprouting, although the cellular signals remain under studied[5,57]. Further highlighting the
405 importance of tSCs for nerve regeneration, a recent study used an anti-GD3 antibody to
406 selectively eliminate tSCs after a peroneal nerve injury. The result was a reduction in the number
407 of tSCs, decreased muscle reinnervation, and impaired functional recovery[6]. Our study
408 significantly expands on these previous studies by providing novel understanding of the role of
409 Spp1-signaling acting on Schwann cells near the NMJ and its importance for the regeneration of
410 NMJs.

411 Our research further highlights the *Sod1*$^{-/-}$ mice as a useful model for understanding NMJ
412 repair processes and tSC responses during the remodeling of innervation. In support of this
413 contention are our observations during the remodeling phase, of key characteristics reminiscent
414 of NMJ regeneration, such as increased AChR area, tSC proliferation[5], polyinnervation[58], and
415 axonal blebbing[59]. Unlike nerve injury, which denervates every fiber leading to a lack of NMJ

416 structural diversity, young *Sod1*$^{-/-}$ mice recapitulate what we postulate to be a more faithful
417 representation of NMJ remodeling in the context of normal aging and/or degenerative
418 neuromuscular diseases. Recognizing the potency of this model for investigating NMJ diversity
419 and the response of muscle-resident Schwann cells to denervation propelled our decision to
420 perform single-cell RNA sequencing (scRNA-Seq) of muscle niche cells, emphasizing GFP+
421 Schwann cells, which identified two distinct subtypes each for myelin Schwann cells and tSCs. A
422 particular tSC subtype demonstrated traits related to ECM organization and synapse promotion
423 and was considerably enriched in the *Sod1*$^{-/-}$ muscles at 2-months of age, supporting their
424 important role in NMJ regeneration.

425 Overall, our research deepens the existing knowledge on the intricate cellular processes
426 of NMJ regeneration orchestrated by Schwann cells. Specifically, we highlight the importance of
427 Spp1 signaling and elucidate the distinct roles played by specialized subtypes of muscle-resident
428 Schwann cells. These insights not only expand our understanding of neuromuscular biology but
429 also present promising avenues for targeted therapeutic strategies. Such innovations hold the
430 potential to revolutionize the treatment landscape for debilitating neuromuscular disorders,
431 including ALS and sarcopenia.

432

433 **Study Approval**

434 All animal experiments were approved by the University of Michigan Institutional Animal Care and
435 Use committee (IACUC)(PRO00008744).

436 **Acknowledgments**

437 This work was supported by the National institutes of Health (NIH) under the awards
438 R01(AG050676) (SVB), P01 (AG051442) (SVB), P30 (AR069620)(SVB), T32 (AG000114)(SDG),
439 and the American Physiological Society Porter Fellowship (SDG).

440 **Conflict of Interest**

441 The authors declare that there are no conflicts of interest.

442 **Methods**

443 **Animal Models.** All experimental procedures were approved by the University of Michigan
444 Institutional Animal Care and Use Committee (PRO00010548) and conducted in accordance with
445 National Institutes of Health guidelines. Animals were sacrificed via intraperitoneal injection of
446 tribromoethanol, followed by administration of a pneumothorax.

447 All mice used for experimentation were bred at the University of Michigan with *Sod1*$^{-/-}$ and
448 WT mice initially provided generously by Dr. Holly Van Remmen while she was at the University
449 of Texas Health Science Center at San Antonio[60]. Mice expressing enhanced Green Fluorescent
450 Protein (GFP) driven by the S100B promoter to visualize Schwann cells (S100GFP-tg Kosmos
451 mice)[14] were generously provided by Dr. Alison Snyder-Warwick at Washington University in St.
452 Louis, MO. *S100GFP*-tg mice were crossed with *Sod1*$^{-/-}$ mice to form a first generation of mice
453 that contained a knockout allele for Sod1 and wild type allele for the Sod1 gene and the S100GFP
454 transgene, S100GFP-tg *Sod1*$^{+/-}$. First generation mice were crossed to generate a second
455 generation of *Sod1*$^{-/-}$ mice expressing GFP under the S100B promoter to be used for our
456 experiments. To maintain a stable colony of *S100GFP*-tg *Sod1*$^{-/-}$ mice, male *S100GFP*-tg *Sod1*$^{-/-}$
457 and female S100GFP-tg *Sod1*$^{+/-}$ mice were consistently bred to produce litters with approximately
458 50% of the mice containing the experimental genotype, *S100GFP*-tg *Sod1*$^{-/-}$. Control mice in this
459 study contain the genotype, S100GFP-tg *Sod1*$^{+/+}$, simply referred to as S100GFP-tg.

460

461 ***In situ* Force Testing.** Mice were anesthetized with initial intraperitoneal injections of Avertin
462 (tribromoethanol, 250 mg/kg) with supplemental injections to maintain an adequate level of
463 anesthesia during all procedures. Gastrocnemius (GTN) or tibialis anterior (TA) muscle contractile
464 properties were measured in situ, as described by Larkin et al. (2011)[61]. In anesthetized mice, the
465 whole GTN or TA muscle was isolated from surrounding muscle and connective tissue using great
466 care not to damage the nerve and/or blood vessels during the dissection. A 4-0 silk suture was
467 tied around the distal tendon and the tendon was severed. The animal was then placed on a

468 temperature-controlled platform warmed to maintain body temperature at 37°C. The hindlimb was
469 secures to the platform, and the tendon was tied to the lever arm of a servomotor (model 6650LR,
470 Cambridge Technology). A continual drip of saline warmed to 37°C was administered to the
471 muscles to maintain temperature. Muscle were activated either by stimulation of the tibial (GTN
472 muscle) or common peroneal (TA muscle) nerve using a bipolar platinum wire electrode or by
473 direct stimulation of the muscle via cuff electrodes wrapped around the proximal and distal ends
474 of the muscle. Custom-designed software (LabVIEW 2018; National Instruments, Austin, TX)
475 controlled electrical pulse properties and servomotor activity and recorded data from the force
476 transducer. The voltage of 0.2 ms stimulus pulses was increased, and optimal muscle length (Lo)
477 was subsequently adjusted, to give maximum twitch force. The Lo was measured with digital
478 calipers. Muscles were held at Lo and subjected to 300 ms trains of pulses with increase
479 stimulation frequencies maximum isometric force (Po) was achieved. Previously established Lf-
480 to-Lo ratios of 0.45 for GTN muscles and 0.6 for TA muscles were used to calculate Lf for each
481 muscle. The physiological cross-sectional area (CSA) of muscles was determined by dividing the
482 mass of the muscle by the product of Lf and 1.06 g/cm3, the density of mammalian skeletal
483 muscle[62]. Po was normalized by the CSA to calculate specific Po (sPo), as a measure of intrinsic
484 force generating capacity. Functional innervation was assessed by calculating the ratio of force
485 production in response to nerve stimulation relative to the force elicited by direct muscle
486 stimulation. A value of 1.0 indicates high fidelity of the nerve-muscle functional connections, while
487 the extent to which the ratio is less than 1.0 provides an indication of the fraction of muscle fibers
488 that are unable to respond to nerve stimulation.
489
490 **Immunofluorescent Staining and Imaging.** Animals were sacrificed and the muscles were fixed
491 in 4% paraformaldehyde (PFA) in PBS for 15 min and sucrose protected overnight with 20%
492 sucrose, followed by embedding in optimal cutting temperature (OCT) compound (Tissue Tek)
493 and stored at -80°C prior to use. For visualization and examination of neuromuscular junction

494 (NMJ) structure, muscles were dissected using fine forceps to tease muscle fibers into layers
495 consisting of a maximum of 10-20 muscle fibers. The samples were then treated with ice cold
496 methanol for 30 seconds, washed 3 times in PBS for 5 min each, then blocked for 30 minutes at
497 room temperature in 5% goat serum, PBS, triton X-100 (0.5%), and 2% bovine serum albumin
498 (BSA). Fab fragments (10% in blocking solution) were used to block endogenous IgG before
499 applying any mouse monoclonal primary antibodies. Muscle fiber bundles were then stained with
500 antibodies and mounted on a slide, and coverslips were applied.

501 Primary antibodies used for this experiment were as follows: a combination of NF and SV2
502 (Developmental Studies Hybridoma Bank) for labeling α-motor axon terminals and axons, anti-
503 S100 (Dako, Z0311) to enhance labeling of all SCs, anti-Ki67 (rat), anti-SPP1 (Abcam, ab8448),
504 and anti-CD44 (Thermo Fisher Scientific, 50-143-16). Secondary antibodies consisted of Alex
505 Fluors that were conjugated to the secondary antibodies (Life Technologies). α-BTX conjugated
506 to Alexa Fluor 555 (Invitrogen, B35451) was used to label the acetylcholine receptors (AChR),
507 and 4′,6-diamidino-2-phenylindole (DAPI) was used to label all nuclei.

508 A Nikon A1 high-sensitivity confocal laser scanning microscope with 40× oil immersion
509 objective was used to capture 16-bit, 512×512-pixel frame size, Z-stack images with 1 μm interval.
510 A minimum of 20-30 NMJs were acquired per animal.

511

512 **NMJ feature quantification.** Fiji software was used for quantitative analysis of confocal
513 micrographs. All analyses were performed on maximum intensity projections using guidelines
514 described in detail in the NMJ-Morph image processing pipeline.[29] The obtained images were
515 preserved as nd2 Nikon files and subsequently imported into ImageJ software, with channels
516 consolidated into a single tiff image prior to their separation for individual component analysis.
517 Initial preparations involved the division and cropping of images to ensure each contained a
518 singular NMJ, enabling individual analysis of each NMJ. The analysis was constrained to en-face
519 NMJs only.

For each channel, a threshold was set using the thresholding tool to produce a binary mask that most closely resembled the real image of the NMJ component being analyzed. The binary mask was selected and measured to provide the area and perimeter of the selected channel (Extended Data Fig 1). The endplate mask was generated by applying the 'Create background' FIJI tool on the AChR mask, which completely fills in the AChR mask. Endplate area and diameter were also measured (Extended Data Fig. 1a). This process was repeated for every NMJ image, for each of the NMJ components.

The 'Overlap' and 'SC Coverage' measurements (Extended Data Fig 1d,e) were derived in accordance to NMJ-Morph guidelines. Briefly, the following calculations were used:

$$Overlap, SC\ Coverage = \left[\frac{AchR\ Area - unoccupied\ area\ of\ AChR}{AChR\ Area}\right] \times 100$$

$$Synaptic, SC\ Coverage\ Area = AchR\ Area - unnocupied\ area\ of\ AChR$$

The unoccupied area denotes regions lacking colocalization with α-BTX. Following the generation of a binary mask for calculating the AChR, nerve teriminal, and tSC areas (Extended Data Fig. 1a-c), the masks were processed, inverted as needed, and merged to measure unoccupied areas of AChR. Beyond structural area measurements, attention was given to NMJs manifesting visible polyinnervation—characterized by the convergence of at least two axons onto a single NMJ (Extended Data Fig. 1f). Furthermore, the presence of axon terminal blebs per NMJ was recorded (Extended Data Fig. 1f).

NMJ UMAP and k-means clustering analysis. Raw data for all sixteen NMJ features described above were imported into *R*. The numeric dataset underwent Z-score normalization through the scale() function in *R*. This normalization ensured a transformation of every individual feature to attain a mean of 0 and a standard deviation of 1, critical for subsequent analyses. Uniform Manifold Approximation and Projection (UMAP) was performed, using the 'umap' package on R,

548 on the scaled data using a fixed seed to ensure reproducibility. An elbow method was utilized to
549 determine the optimal number of clusters[63]. Within-cluster sum of squares was computed for each
550 'k', and an elbow curve was plotted to visually inspect the optimal number of clusters. After re-
551 establishing the seed to maintain result consistency during k-means clustering, four was
552 established as the optimal number of clusters. Using the kmeans() function in *R* each NMJ was
553 assigned to a specific cluster. The generated clusters were then visualized and overlaid on the
554 original UMAP plot to depict the identified groupings distinctly. All plots were generated using
555 ggplot2.
556
557 **Quantification of Perisynaptic and Extrasynaptic Ki67+ Nuclei.** Muscle fiber bundles from 2-
558 month-old *S100GFP*-tg and *S100GFP*-tg *Sod1*$^{-/-}$ were processed and stained with anti-Ki67,
559 DAPI, α-BTX, and anti-S100B to delineate nuclei and cellular structures. Confocal imaging was
560 performed using a Nikon A1 microscope, with images captured at 20X and 40X magnifications.
561 The imaging focused on fields containing NMJs along with visualization of the surrounding areas.
562 Classification of perisynaptic Ki67+ nuclei involved those being DAPI+ Ki67+ and overlapping
563 with α-BTX stain. Perisynaptic Ki67+ GFP+ nuclei were identified as DAPI+ Ki67+ S100GFP+
564 and overlapping with an endplate (α-BTX stain). Extrasynaptic Ki67+ nuclei were those located
565 within 50 μm from the nearest endplate. The quantification was normalized by the number of
566 NMJs per image field to ensure comparability across different fields and conditions.
567
568 **Single cell isolation via FACS.** For tissue collection, mice were anesthetized with 3% isoflurane,
569 then euthanized by cervical dislocation, bilateral pneumothorax, and removal of the heart. Hind
570 limb muscles (TA and GTN) of control and experimental mice were quickly harvested using sterile
571 surgical tools and placed in separate plastic petri dishes containing cold phosphate-buffered
572 saline (PBS). Using surgical scissors, muscle tissues were minced and transferred into 50 mL
573 conical tubes containing 20 mL of digest solution (2.5 U/mL Dispase II and 0.2% [~1000 U/mL]

574 Collagenase Type II, 1 mg/mL of hyaluronidase in Dulbecco's modified Eagle medium [DMEM]
575 per mouse). Samples were incubated on a rocker placed in a 37℃ incubator for 60 min with
576 manual pipetting the solution up and down to break up tissue every 30 min using an FBS-coated
577 10 mL serological pipette. Once the digestion was completed, 20 mL of F12 media containing
578 20% heat inactivated FBS was added into each sample to inactivate enzyme activity. The solution
579 was then filtered through a 70 mm cell strainer into a new 50 mL conical tube and centrifuged
580 again at 300g for 5 min. Live cells were sorted from the suspension via addition of 1 μg of
581 propidium iodide (PI) stain into each experimental sample and all samples were filtered through
582 70 mm cell strainers before the FACS. Cell sorting was done using a BD FACS Aria III Cell Sorter
583 (BD Biosciences, San Jose, CA). GFP+ PI- and GFP- PI- cells were sorted into 0.02% BSA PBS
584 solution for immediate processing.
585
586 **scRNA sequencing.** Freshly isolated single cells were sorted into staining solution, enumerated
587 by hemocytometer, and re- suspended into PBS. Cells were loaded into the 10X Genomics
588 chromium single cell controller for each sample and captured into nanoliter-scale gel bead-in-
589 emulsions. cDNAs were prepared using the single cell 30 Protocol as per manufacturer's
590 instructions and sequenced on a NovaSeq instrument (Illumina) with 26 bases for read 1 and 98
591 bases for read 2.
592
593 **scRNA-Seq data processing and analysis.** Cell Ranger 7.1.0 (10X Genomics) was used to
594 process raw data. The CellRanger workflow aligns sequencing reads to the mm10 transcriptome
595 using the STAR aligner and exports count data[64]. The CellRanger count command was run with
596 default parameters. Filtered feature barcode data were imported into Seurat (v4.3)[65]. Ambient
597 RNA was removed using Decontx[66] and only cells with greater than 200 genes and <10%
598 mitochondrial reads were included in our analysis. Scaling, normalization, variable gene selection,
599 dimensionality reduction, and clustering were performed with default settings using the Seurat.

600 Cell types were assigned to each cluster using known marker genes. Pathway analysis was
601 performed using enrichGO() function in clusterProfiler[67] with the default parameters and used
602 gene markers that were upregulated (log2FC > 1) in the tSC-B cluster compared to all other
603 muscle-resident Schwann cells as the gene list. Upregulated genes were determined using the
604 FindMarkers() function in Seurat. Secreted signaling intercellular interaction analysis was
605 performed using the CellChat package with standard parameters and setting the CellChat
606 database to "Secreted Signaling".[40]
607
608 **Whole-tissue RNA extraction and RT-qPCR Analysis.** GTN and TA muscle samples were
609 homogenized in TRIzol reagent (Invitrogen, Thermo Fisher Scientific) using a bead mill. RNA was
610 isolated by phenol/chloroform extraction and RNA yield was determined using a NanoDrop
611 Spectrophotometer (NanoDrop 2000c, Thermo Fisher Scientific). Genomic DNA was removed by
612 incubation with DNase I (Ambion, Thermo Fisher Scientific, AM2222) followed by its heat
613 inactivation. Total RNA (1 µg) was reverse-transcribed to cDNA using SuperScript III Master Mix,
614 Random Hexamers, and dNTPs (Invitrogen, Thermo Fisher Scientific) and RT-qPCR performed
615 on a CFX96 Real-Time PCR Detection System (Bio-Rad, 1855195) in triplicate 20 µL reactions
616 of iTaq Universal SYBR Green Supermix (Bio-Rad, 1725124) with 1 µM forward and reverse
617 primer. Relative mRNA expression was determined using the $2^{-\Delta\Delta CT}$ method with Gapdh serving
618 as a control for the samples.
619
620 **Nerve injuries and neutralization of intramuscular Spp1.** Male C57BL/6J mice, aged between
621 10 - 16 weeks, were subjected to bilateral sciatic or peroneal nerve crush to induce muscle
622 denervation in both legs. Forceps were employed to produce the crush. Mice assigned to sciatic
623 nerve injury protocols had tissues harvested at intervals of 0, 7, 14, or 28 days following the injury.
624 For those undergoing peroneal nerve injury, a 10 µL intramuscular injection of Spp1 neutralizing
625 antibody (4 µg, AF808, R&D Systems) was administered into the tibialis anterior (TA) muscles,

utilizing a Hamilton syringe. This injection routine was repeated every two days post the initial injury. Control mice received saline injections concurrent with the day of injury and repeated every two days thereafter. Seven days post injury (DPI), all mice were anesthetized and TA muscles were assessed for contractile functionality and collected for NMJ imaging.

Statistical analysis. Data are presented as the mean ± SEM**.** All statistical analyses were performed using GraphPad Prism 8 (GraphPad Software) and *R*. Between-group differences were tested by two-tailed unpaired students t-tests (2 groups) or by a one-way analysis of variance (ANOVA) followed by Dunnett's multiple comparisons test. A two-way ANOVA followed by Tukey's multiple comparison's test was executed when two factors were involved. Differences were considered to be statistically significant at the $P < 0.05$ level (*$p < 0.05$, **$p<0.01$, ***$p < 0.001$, ns: not significant).

652 **References**

653 1. Fischer, L. R. *et al.* Amyotrophic lateral sclerosis is a distal axonopathy: Evidence in mice
654 and man. *Exp Neurol* **185**, 232–240 (2004).
655 2. Killian, J. M., Wilfong, A. A., Burnett, L., Appel, S. H. & Boland, D. Decremental motor
656 responses to repetitive nerve stimulation in ALS. *Muscle Nerve* **17**, 747–754 (1994).
657 3. Moreira-Pais, A., Ferreira, R., Oliveira, P. A. & Duarte, J. A. A neuromuscular perspective
658 of sarcopenia pathogenesis: deciphering the signaling pathways involved. *Geroscience*
659 **44**, 1199–1213 (2022).
660 4. Santosa, K. B., Keane, A. M., Jablonka-Shariff, A., Vannucci, B. & Snyder-Warwick, A. K.
661 Clinical relevance of terminal Schwann cells: An overlooked component of the
662 neuromuscular junction. *Journal of Neuroscience Research* vol. 96 1125–1135 Preprint at
663 https://doi.org/10.1002/jnr.24231 (2018).
664 5. Love, F. M. & Thompson, W. J. *Schwann Cells Proliferate at Rat Neuromuscular*
665 *Junctions during Development and Regeneration*. (1998).
666 6. Jablonka-Shariff, A., Balta, E., Santosa, K. B., Lu, C. Y. & Snyder-Warwick, A. K.
667 Terminal Schwann Cells Are Essential for Neuromuscular Junction Function and
668 Recovery after Nerve Injury. *Plast Reconstr Surg* **151**, 792–803 (2023).
669 7. Ahn, B. *et al.* Scavenging mitochondrial hydrogen peroxide by peroxiredoxin 3
670 overexpression attenuates contractile dysfunction and muscle atrophy in a murine model
671 of accelerated sarcopenia. *Aging Cell* **21**, (2022).
672 8. Su, Y. *et al.* Transgenic expression of SOD1 specifically in neurons of Sod1 deficient
673 mice prevents defects in muscle mitochondrial function and calcium handling. *Free Radic*
674 *Biol Med* **165**, 299–311 (2021).
675 9. Larouche, J. A. *et al.* Murine muscle stem cell response to perturbations of the
676 neuromuscular junction are attenuated with aging. *Elife* **10**, (2021).
677 10. Sataranatarajan, K. *et al.* Molecular changes in transcription and metabolic pathways
678 underlying muscle atrophy in the CuZnSOD null mouse model of sarcopenia.
679 *Geroscience* **42**, 1101–1118 (2020).
680 11. Muller, F. L. *et al.* Denervation-induced skeletal muscle atrophy is associated with
681 increased mitochondrial ROS production. *Am J Physiol Regul Integr Comp Physiol* **293**,
682 1159–1168 (2007).
683 12. Goldman, D., Brenner, H. R. & Heinemann, S. *Acetylcholine Receptor a-, p-, y-, and*
684 *&Subunit mRNA levels Are Regulated by Muscle Activity*. *Neuron* vol. 1 (1988).
685 13. Ma, J. *et al.* Gene expression of myogenic regulatory factors, nicotinic acetylcholine
686 receptor subunits, and GAP-43 in skeletal muscle following denervation in a rat model.
687 *Journal of Orthopaedic Research* **25**, 1498–1505 (2007).
688 14. Zuo, Y. *et al.* Fluorescent Proteins Expressed in Mouse Transgenic Lines Mark Subsets
689 of Glia, Neurons, Macrophages, and Dendritic Cells for Vital Examination. *Journal of*
690 *Neuroscience* **24**, 10999–11009 (2004).
691 15. Personius, K. E. & Sawyer, R. P. Variability and failure of neurotransmission in the
692 diaphragm of mdx mice. *Neuromuscular Disorders* **16**, 168–177 (2006).
693 16. Missias, A. C., Chu, G. C., Klocke, B. J., Sanes, J. R. & Merlie, J. P. Maturation of the
694 Acetylcholine Receptor in Skeletal Muscle: Regulation of the AChR γ-to-ϵ Switch. *Dev*
695 *Biol* **179**, 223–238 (1996).
696 17. Bezakova, G. & Ruegg, M. A. New insights into the roles of agrin. *Nature Reviews*
697 *Molecular Cell Biology 2003 4:4* **4**, 295–309 (2003).
698 18. Boyd, J. G. & Gordon, T. Neurotrophic Factors and Their Receptors in Axonal
699 Regeneration and Functional Recovery after Peripheral Nerve Injury. *Mol Neurobiol* **27**,
700 277–323 (2003).

701 19. Trupp, M. *et al.* Peripheral expression and biological activities of GDNF, a new
702 neurotrophic factor for avian and mammalian peripheral neurons. *Journal of Cell Biology*
703 **130**, 137–148 (1995).
704 20. Gerdes, J. *et al. CELL CYCLE ANALYSIS OF A CELL PROLIFERATION-ASSOCIATED*
705 *HUMAN NUCLEAR ANTIGEN DEFINED BY THE MONOCLONAL ANTIBODY Ki-67'*.
706 *THE JOURNAL OF IMMUNOLOGY* vol. 133 http://journals.aai.org/jimmunol/article-
707 pdf/133/4/1710/1031649/1710.pdf (1984).
708 21. Sherr, C. J. D-type cyclins. *Trends Biochem Sci* **20**, 187–190 (1995).
709 22. Atanasoski, S., Shumas, S., Dickson, C., Scherer, S. S. & Suter, U. Differential Cyclin D1
710 Requirements of Proliferating Schwann Cells during Development and after Injury.
711 *Molecular and Cellular Neuroscience* **18**, 581–592 (2001).
712 23. Britsch, S. *et al.* The transcription factor Sox10 is a key regulator of peripheral glial
713 development. *Genes Dev* **15**, 66–78 (2001).
714 24. Perry, V. H., Brown, M. C. & Gordon, S. BriefDefinitive Report THE MACROPHAGE
715 RESPONSE TO CENTRAL AND PERIPHERAL NERVE INJURY A Possible Role for
716 Macrophages in Regeneration.
717 25. Duregotti, E. *et al.* Mitochondrial alarmins released by degenerating motor axon terminals
718 activate perisynaptic schwann cells. *Proc Natl Acad Sci U S A* **112**, E497–E505 (2015).
719 26. Aigner, L. *et al. Overexpression of the Neural Growth-Associated Protein GAP-43*
720 *Induces Nerve Sprouting in the Adult Nervous System of Transgenic Mice*. *Cell* vol. 83
721 (1995).
722 27. Serafini, T. *et al.* The netrins define a family of axon outgrowth-promoting proteins
723 homologous to C. elegans UNC-6. *Cell* **78**, 409–424 (1994).
724 28. Petrenko, V., Mihhailova, J., Salmon, P. & Kiss, J. Z. Apoptotic neurons induce
725 proliferative responses of progenitor cells in the postnatal neocortex. *Exp Neurol* **273**,
726 126–137 (2015).
727 29. Jones, R. A. *et al.* Correction to NMJ-morph reveals principal components of synaptic
728 morphology influencing structure - Function relationships at the neuromuscular junction
729 (Open Biology (2016) 6 (160240) DOI: 10.1098/rsob.160335). *Open Biology* vol. 7
730 Preprint at https://doi.org/10.1098/rsob.160240 (2017).
731 30. Gerber, D. *et al.* Transcriptional profiling of mouse peripheral nerves to the single-cell
732 level to build a sciatic nerve atlas (Snat). *Elife* **10**, (2021).
733 31. Castro, R. *et al.* Specific labeling of synaptic schwann cells reveals unique cellular and
734 molecular features. *Elife* **9**, (2020).
735 32. Proietti, D. *et al.* Activation of skeletal muscle-resident glial cells upon nerve injury. *JCI*
736 *Insight* **6**, (2021).
737 33. Procacci, N. M. *et al.* Kir4.1 is specifically expressed and active in non-myelinating
738 Schwann cells. *Glia* **71**, 926–944 (2023).
739 34. Glass, D. J. *et al.* Agrin acts via a MuSK receptor complex. *Cell* **85**, 513–523 (1996).
740 35. Gorlewicz, A. *et al.* CD44 is expressed in non-myelinating Schwann cells of the adult rat,
741 and may play a role in neurodegeneration-induced glial plasticity at the neuromuscular
742 junction. *Neurobiol Dis* **34**, 245–258 (2009).
743 36. Lee, K. E. *et al.* Positive feedback loop between Sox2 and Sox6 inhibits neuronal
744 differentiation in the developing central nervous system. *Proc Natl Acad Sci U S A* **111**,
745 2794–2799 (2014).
746 37. Stolt, C. C. *et al.* SoxD Proteins Influence Multiple Stages of Oligodendrocyte
747 Development and Modulate SoxE Protein Function. *Dev Cell* **11**, 697–709 (2006).
748 38. Ittner, E. *et al.* SoxD transcription factor deficiency in Schwann cells delays myelination in
749 the developing peripheral nervous system. *Sci Rep* **11**, (2021).
750 39. Xie, Z. *et al.* Cellular and subcellular localization of PDE10A, a striatum-enriched
751 phosphodiesterase. *Neuroscience* **139**, 597–607 (2006).

40. Jin, S. *et al.* Inference and analysis of cell-cell communication using CellChat. *Nat Commun* **12**, (2021).
41. Wang, J. B. *et al.* SPP1 promotes Schwann cell proliferation and survival through PKCα by binding with CD44 and αvβ3 after peripheral nerve injury. *Cell Biosci* **10**, (2020).
42. Pegoraro, E. *et al.* SPP1 genotype is a determinant of disease severity in Duchenne muscular dystrophy. *Neurology* **76**, 219–226 (2011).
43. Liu, L. *et al.* Exercise reprograms the inflammatory landscape of multiple stem cell compartments during mammalian aging. *Cell Stem Cell* **30**, 689-705.e4 (2023).
44. Vetrone, S. A. *et al.* Osteopontin promotes fibrosis in dystrophic mouse muscle by modulating immune cell subsets and intramuscular TGF-β. *Journal of Clinical Investigation* **119**, 1583–1594 (2009).
45. Coulis, G. *et al. Single-cell and spatial transcriptomics identify a macrophage population associated with skeletal muscle fibrosis*. https://www.science.org (2023).
46. Li, S. & Jakobs, T. C. Secreted phosphoprotein 1 slows neurodegeneration and rescues visual function in mouse models of aging and glaucoma. *Cell Rep* **41**, (2022).
47. Shen, Y., Mani, S., Donovan, S. L., Schwob, J. E. & Meiri, K. F. Growth-Associated Protein-43 Is Required for Commissural Axon Guidance in the Developing Vertebrate Nervous System. *Journal of Neuroscience* **22**, 239–247 (2002).
48. Hung, C. C. *et al.* Astrocytic GAP43 Induced by the TLR4/NF-κB/STAT3 Axis Attenuates Astrogliosis-Mediated Microglial Activation and Neurotoxicity. *Journal of Neuroscience* **36**, 2027–2043 (2016).
49. Woolf, C. J. *et al. Denervation of the Motor Endplate Results in the Rapid Expression by Terminal Schwann Cells of the Growth-associated Protein GAP-43*. *The Journal of Neuroscience* vol. 12 (1992).
50. Watson, D. C. *et al.* GAP43-dependent mitochondria transfer from astrocytes enhances glioblastoma tumorigenicity. *Nat Cancer* **4**, 648–664 (2023).
51. Smith, G. M. & Gallo, G. The role of mitochondria in axon development and regeneration. *Dev Neurobiol* **78**, 221–237 (2018).
52. Lv, J. *et al.* Netrin-1 induces the migration of Schwann cells via p38 MAPK and PI3K-Akt signaling pathway mediated by the UNC5B receptor. *Biochem Biophys Res Commun* **464**, 263–268 (2015).
53. Dun, X. P. & Parkinson, D. B. Role of Netrin-1 Signaling in Nerve Regeneration. *International Journal of Molecular Sciences 2017, Vol. 18, Page 491* **18**, 491 (2017).
54. Meltzer, S. *et al.* A role for axon-glial interactions and Netrin-G1 signaling in the formation of low-threshold mechanoreceptor end organs. (2022) doi:10.1073/pnas.
55. Siironen, J., Collan, Y. & Röyttä, M. Axonal reinnervation does not influence Schwann cell proliferation after rat sciatic nerve transection. *Brain Res* **654**, 303–311 (1994).
56. Yang, D. P. *et al.* Schwann cell proliferation during Wallerian degeneration is not necessary for regeneration and remyelination of the peripheral nerves: Axon-dependent removal of newly generated Schwann cells by apoptosis. *Molecular and Cellular Neuroscience* **38**, 80–88 (2008).
57. Kang, H., Tian, L., Mikesh, M., Lichtman, J. W. & Thompson, W. J. Terminal schwann cells participate in neuromuscular synapse remodeling during reinnervation following nerve injury. *Journal of Neuroscience* **34**, 6323–6333 (2014).
58. Vannucci, B. *et al.* What is Normal? Neuromuscular junction reinnervation after nerve injury. *Muscle Nerve* **60**, 604–612 (2019).
59. Taetzsch, T. & Valdez, G. NMJ maintenance and repair in aging. *Current Opinion in Physiology* vol. 4 57–64 Preprint at https://doi.org/10.1016/j.cophys.2018.05.007 (2018).
60. Huang, T.-T. *et al. Superoxide-Mediated Cytotoxicity in Superoxide Dismutase-Deficient Fetal Fibroblasts The importance of CuZnSOD and MnSOD in pro*. *ARCHIVES OF BIOCHEMISTRY AND BIOPHYSICS* vol. 344 (1997).

61. Larkin, L. M. *et al.* Skeletal muscle weakness due to deficiency of CuZn-superoxide dismutase is associated with loss of functional innervation. *Am J Physiol Regul Integr Comp Physiol* **301**, R1400-7 (2011).
62. Burkholder, T. J., Fingado, B., Baron, S. & Lieber, R. L. Relationship between muscle fiber types and sizes and muscle architectural properties in the mouse hindlimb. *J Morphol* **221**, 177–190 (1994).
63. Humaira, H. & Rasyidah, R. Determining The Appropiate Cluster Number Using Elbow Method for K-Means Algorithm. in (European Alliance for Innovation n.o., 2020). doi:10.4108/eai.24-1-2018.2292388.
64. Dobin, A. *et al.* STAR: ultrafast universal RNA-seq aligner. *Bioinformatics* **29**, 15–21 (2013).
65. Butler, A., Hoffman, P., Smibert, P., Papalexi, E. & Satija, R. Integrating single-cell transcriptomic data across different conditions, technologies, and species. *Nature Biotechnology 2018 36:5* **36**, 411–420 (2018).
66. Yang, S. *et al.* Decontamination of ambient RNA in single-cell RNA-seq with DecontX. *Genome Biol* **21**, (2020).
67. Wu, T. *et al.* clusterProfiler 4.0: A universal enrichment tool for interpreting omics data. *The Innovation* **2**, 100141 (2021).

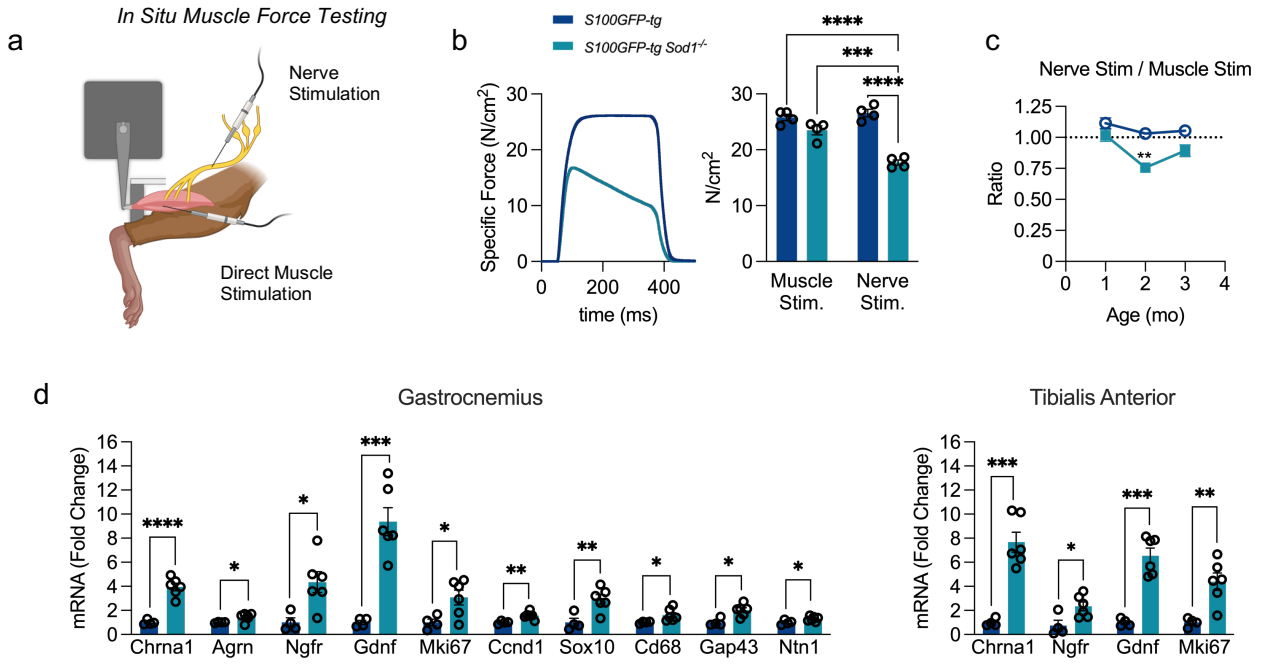

Fig. 1| Muscle mechanics and transcriptional profiling of canonical markers reveals a marked but transient denervation/reinnervation response in young *S100GFP*-tg *Sod1*$^{-/-}$ mice. a, Illustration of in situ muscle force testing protocol used to determine NMJ transmission. Evoked muscle forces were evaluated in gastrocnemius (GTN) muscles from anesthetized mice by stimulating directly at the muscle or by indirect stimulation of the sciatic nerve. **b**, Representative force traces for muscles of *S100GFP*-tg (blue) and *S100GFP*-tg *Sod1*$^{-/-}$ (teal) mice. Specific forces (N/cm^2) (n = 4 per genotype) evoked during maximum tetanic contractions. **c**, Ratio of maximum isometric forces elicited by nerve stimulation relative to direct muscle stimulation across 1-3 months of age in *S100GFP*-tg *Sod1*$^{-/-}$ (n = 3-5) and *S100GFP*-tg control mice (n = 3-5). **d**, RT-qPCR of canonical markers of NMJ regeneration, Schwann cell repair activation, cell proliferation, and axonal projection in whole GTN (n = 4-6) and tibialis anterior (TA) muscles (n = 4-6) of *S100GFP*-tg *Sod1*$^{-/-}$ and *S100GFP*-tg control mice. Open circles indicate values for each individual mouse and bars represent the mean response ± SEM. *P ≤ 0.05, **P ≤ 0.01, ***P ≤ 0.001, ****P ≤ 0.0001 *S100GFP*-tg vs *S100GFP*-tg *Sod1*$^{-/-}$ by two tailed unpaired t-test or 1-way ANOVA for multiple comparisons.

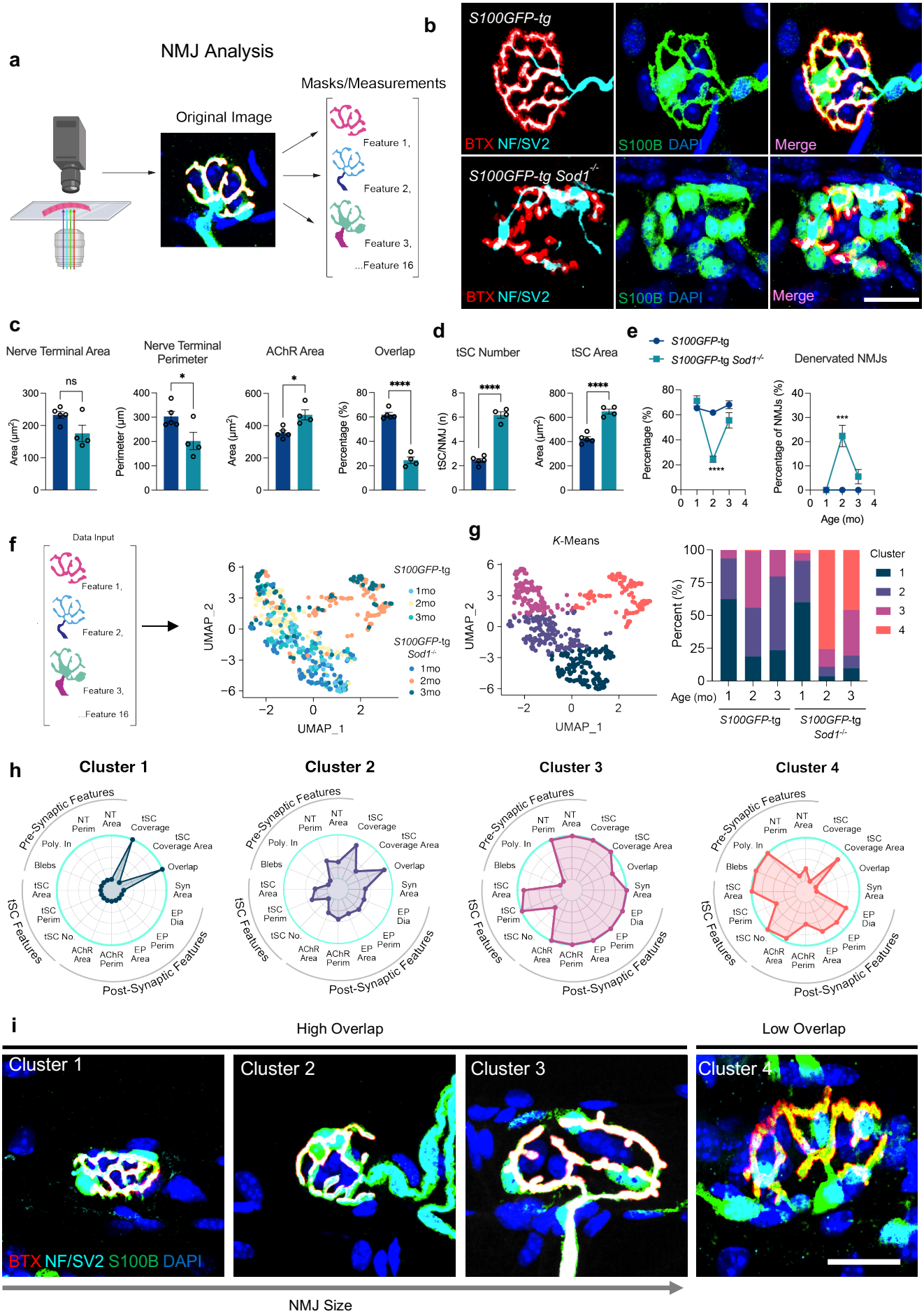
a
NMJ Analysis
Original Image
Masks/Measurements
Feature 1,
Feature 2,
Feature 3,
...Feature 16
b
S100GFP-tg
BTX NF/SV2
S100B DAPI
Merge
S100GFP-tg Sod1-/-
c
Nerve Terminal Area
Nerve Terminal Perimeter
AChR Area
Overlap
d
tSC Number
tSC Area
e
S100GFP-tg
S100GFP-tg Sod1-/-
Denervated NMJs
Age (mo)
f
Data Input
UMAP_1
UMAP_2
1mo
2mo
3mo
g
K-Means
Percent (%)
Cluster
h
Cluster 1
Cluster 2
Cluster 3
Cluster 4
Pre-Synaptic Features
Post-Synaptic Features
tSC Features
i
High Overlap
Low Overlap
BTX NF/SV2 S100B DAPI
NMJ Size

Fig. 2| The remodeling of neuromuscular junctions (NMJs) is associated with greater tSC numbers and larger synaptic areas in *S100GFP*-tg *Sod1*$^{-/-}$ mice. a, Schematic of NMJ analysis – consisting of collecting NMJs images from muscle fiber bundles followed by the generation of feature masks and their measurements. Additional details on the generation of the masks is provided in Extended Data Figure 1 and Methods. **b**, NMJs stained with S100B (Schwann cells; Green), NF/SV2 (Nerve; Cyan), bungarotoxin (AChR; Red), and DAPI (nucleus; Blue) in 2-month-old *S100GFP*-tg control and *S100GFP*-tg *Sod1*$^{-/-}$ mice. **c,d,** Quantification of nerve terminal area, nerve terminal perimeter, AChR area, percentage overlap between AChR area and nerve terminal area, and tSC number and tSC area. **e**, Overlap between nerve terminal and AChR and the % of denervated NMJs for muscles of *S100GFP*-tg and *S100GFP*-tg *Sod1*$^{-/-}$ mice from 1-3 months of age. **f**, The 16 distinct morphological features from all NMJs (n = 522) across all recorded timepoints and genotypes were used to generate a UMAP visualization of the heterogeneity of NMJ structure. **g**, UMAP displayed using k-means clustering and the percentage of clusters represented across all animal groups. **h,** Radar plots indicating the NMJ features (n = 16) profiled across the four identified clusters. The innermost radius of the plot indicates a value of "0" representing the smallest relative mean value across all clusters, whereas the outermost cyan colored circle represents "1" - the maximum relative mean value for a specified feature. Values for all features across all NMJs analyzed are provided in Extended Data Figure 1. **i**, Representative NMJs in clusters 1-4. Open circles indicate average for each individual mouse of no fewer than 20 NMJs analyzed per muscle and bars represent means across animals ± SEM. *Denotes $p < 0.05$ vs *S100GFP*-tg *Sod1*$^{-/-}$ by two tailed unpaired t-test. Scale bar equals 25 µm and images constrained to the same dimensions.

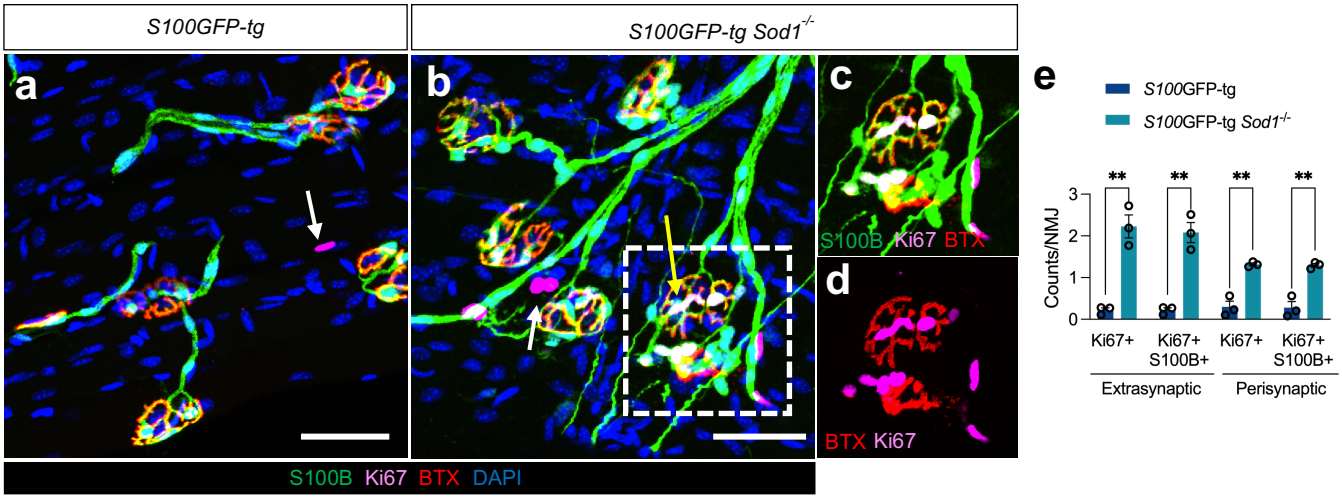

Fig. 3| Enhanced proliferation of tSCs at the NMJ in 2-month-old *S100GFP*-tg *Sod1*$^{-/-}$ mice. Muscle fiber imaging from *S100GFP*-tg (**a**) and *S100GFP*-tg *Sod1*$^{-/-}$ (**b**) mice, immunostained for S100B (green), Ki67 (magenta), α-bungarotoxin (red), and DAPI (blue). White arrows point to extrasynaptic nuclei positive for Ki67 but lacking GFP, while the yellow arrow highlights a perisynaptic Ki67+GFP+ nucleus. **c**, Enlarged view of two NMJs from the highlighted region in b, detailing the S100B, Ki67, and BTX stains. **d**, The same NMJs from c, but focused on BTX and Ki67, revealing multiple Ki67+ nuclei in close proximity to the endplate. **e**, Quantification of extraysnaptic and perisynaptic nuclei either singly labeled for Ki67 or double labeled for Ki67 and GFP. A minimum of 50 NMJs were used per animal. Open circles indicate average values for each individual mouse and bars show the means across animals ± SEM. **Denotes $p < 0.01$ vs *S100GFP*-tg *Sod1*$^{-/-}$ by two tailed unpaired t-test. Scale bars equals 50 µm.

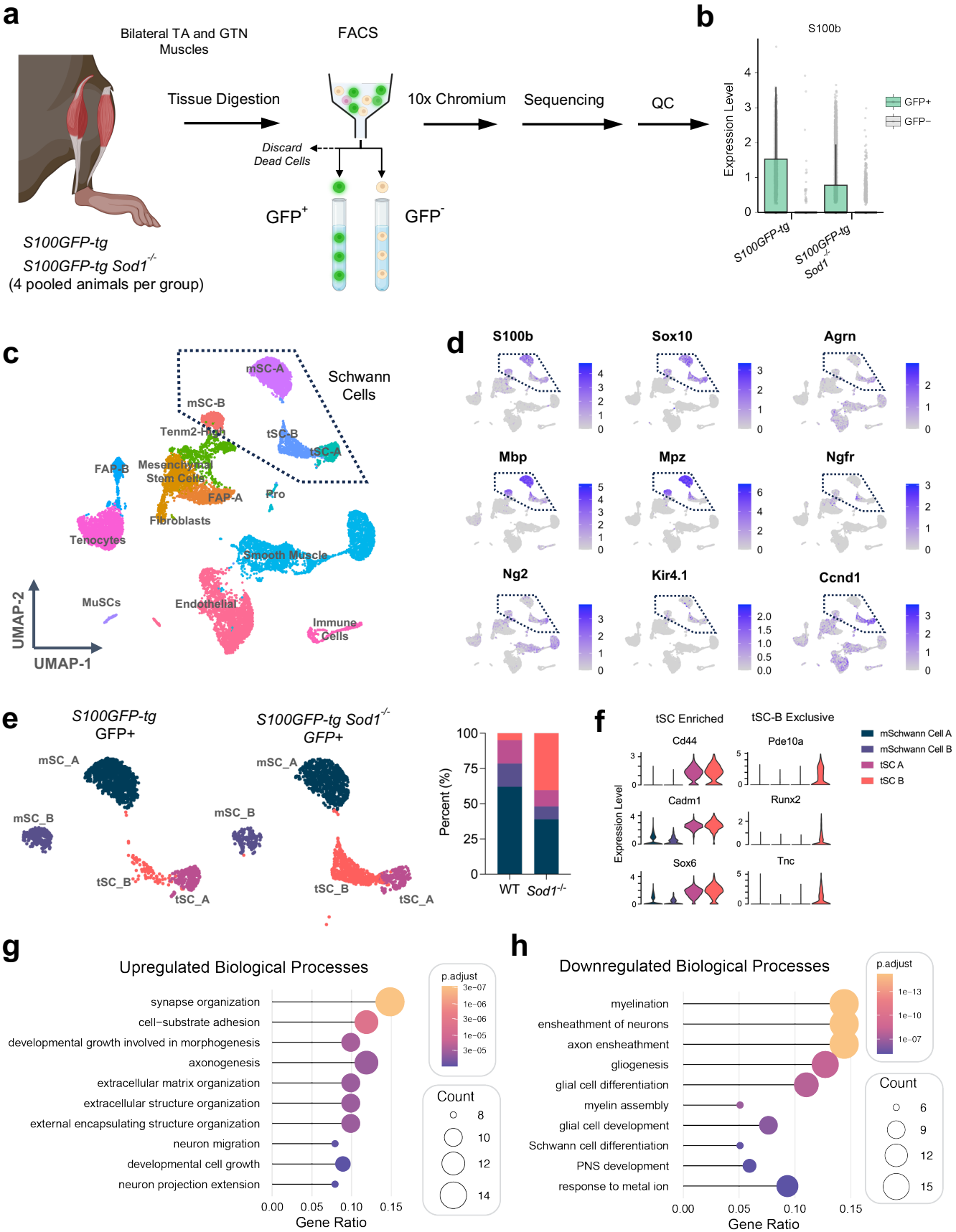
a
Bilateral TA and GTN Muscles
FACS
Tissue Digestion
10x Chromium
Sequencing
QC
Discard Dead Cells
GFP+
GFP-
S100GFP-tg
S100GFP-tg Sod1-/-
(4 pooled animals per group)
b
S100b
Expression Level
GFP+
GFP−
S100GFP-tg
S100GFP-tg Sod1-/-
c
Schwann Cells
mSC-A
mSC-B
Tenm2-High
tSC-B
tSC-A
FAP-B
Mesenchymal Stem Cells
FAP-A
Pro
Fibroblasts
Tenocytes
Smooth Muscle
MuSCs
Endothelial
Immune Cells
UMAP-2
UMAP-1
d
S100b
Sox10
Agrn
Mbp
Mpz
Ngfr
Ng2
Kir4.1
Ccnd1
e
S100GFP-tg GFP+
S100GFP-tg Sod1-/- GFP+
mSC_A
mSC_B
tSC_B
tSC_A
Percent (%)
WT
Sod1-/-
f
tSC Enriched
tSC-B Exclusive
Cd44
Pde10a
Cadm1
Runx2
Sox6
Tnc
Expression Level
mSchwann Cell A
mSchwann Cell B
tSC A
tSC B
g
Upregulated Biological Processes
synapse organization
cell−substrate adhesion
developmental growth involved in morphogenesis
axonogenesis
extracellular matrix organization
extracellular structure organization
external encapsulating structure organization
neuron migration
developmental cell growth
neuron projection extension
Gene Ratio
p.adjust
Count
h
Downregulated Biological Processes
myelination
ensheathment of neurons
axon ensheathment
gliogenesis
glial cell differentiation
myelin assembly
glial cell development
Schwann cell differentiation
PNS development
response to metal ion
Gene Ratio
p.adjust
Count

Fig. 4| Identification of diverse muscle-resident Schwann cell subtypes via single cell RNA-Sequencing (scRNA-Seq). a, Schematic outline of the experimental design: bilateral gastrocnemius (GTN) (n = 8) and tibialis anterior (TA) (n = 8) muscles were harvested from 2-month-old *S100GFP*-tg (n = 4) and *S100GFP*-tg *Sod1*$^{-/-}$ mice (n = 4), subjected to FACS to isolate live GFP+ and GFP- cells, followed by library preparation with 10X Chromium, scRNA-Seq, and quality control (QC). **b,** S100b expression plot across GFP+ and GFP- groups. **c,** UMAP reduction of resulting clusters. In total, 15 clusters were classified. Notably, four distinct clusters of muscle-resident Schwann cells were identified. **d,** UMAP plots illustrating the transcript levels of markers for pan-Schwann cells (S100b, Sox10), myelin Schwann cells (Mbp, Mpz), terminal Schwann cells (Agrn, Ng2, Kir4.1), proliferation (Ccnd1), and a SC repair phenotype (Ngfr). **e,** UMAP plot and quantification (%) of GFP+ muscle-resident Schwann cells. Cluster analysis determined two myelin Schwann cell clusters (mSC-A and mSC-B) and two tSC clusters (tSC-A and tSC-B). **f**, Expression plots displaying markers highly expressed in tSCs (Cd44, Cadm1, Sox6) and exclusive to tSC-B (Pde10a, Runx2, Tnc). **g**, Upregulated and **h,** downregulated biological processes in tSC-B compared to tSC-A and myelin Schwann cells. Pathway descriptions correspond to gene ontology terms representing distinct biological processes. See Extended Data Fig. 3 for genes contributing to upregulated pathways.

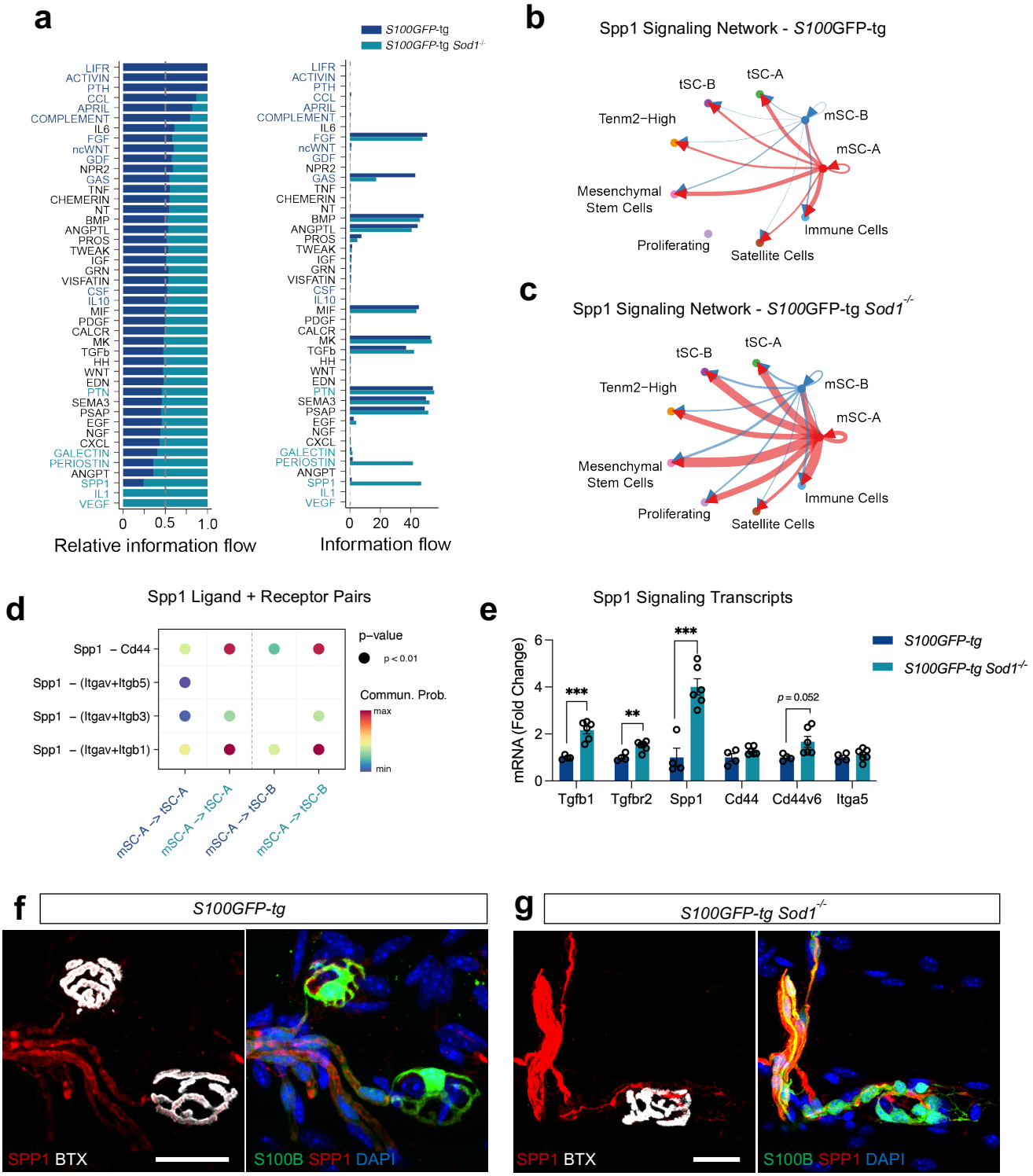
a
S100GFP-tg
S100GFP-tg Sod1-/-
LIFR
ACTIVIN
PTH
CCL
APRIL
COMPLEMENT
IL6
FGF
ncWNT
GDF
NPR2
GAS
TNF
CHEMERIN
NT
BMP
ANGPTL
PROS
TWEAK
IGF
GRN
VISFATIN
CSF
IL10
MIF
PDGF
CALCR
MK
TGFb
HH
WNT
EDN
PTN
SEMA3
PSAP
EGF
NGF
CXCL
GALECTIN
PERIOSTIN
ANGPT
SPP1
IL1
VEGF
0 0.5 1.0
Relative information flow
0 20 40
Information flow
b
Spp1 Signaling Network - S100GFP-tg
tSC-B
tSC-A
Tenm2−High
mSC-B
mSC-A
Mesenchymal Stem Cells
Immune Cells
Proliferating
Satellite Cells
c
Spp1 Signaling Network - S100GFP-tg Sod1-/-
tSC-B
tSC-A
Tenm2−High
mSC-B
mSC-A
Mesenchymal Stem Cells
Immune Cells
Proliferating
Satellite Cells
d
Spp1 Ligand + Receptor Pairs
Spp1 – Cd44
Spp1 – (Itgav+Itgb5)
Spp1 – (Itgav+Itgb3)
Spp1 – (Itgav+Itgb1)
mSC-A –> tSC-A
mSC-A –> tSC-A
mSC-A –> tSC-B
mSC-A –> tSC-B
p–value
p < 0.01
Commun. Prob.
max
min
e
Spp1 Signaling Transcripts
mRNA (Fold Change)
0
2
4
6
***
**
***
p = 0.052
Tgfb1
Tgfbr2
Spp1
Cd44
Cd44v6
Itga5
S100GFP-tg
S100GFP-tg Sod1-/-
f
S100GFP-tg
SPP1 BTX
S100B SPP1 DAPI
g
S100GFP-tg Sod1-/-
SPP1 BTX
S100B SPP1 DAPI

Fig. 5| Intercellular communication infers an Spp1 signaling dynamic between mSC and tSC. a, Secreted signaling pathways enriched in the muscle-resident SC network in *S100GFP*-tg and *S100GFP*-tg *Sod1*$^{-/-}$ mice. Dashed line through the middle on the 'Relative Information Flow' plot represents equal probability that a signaling pathway is active in both groups. Deviations away from the dashed line indicate greater information flow for a specific group. Information flow plot shows the strength of a specific signaling pathway in the overall signaling landscape **b, c,** Circle plots displaying the Spp1 signaling network across cell clusters for (**b**) *S100GFP*-tg and (**c**) *S100GFP*-tg *Sod1*$^{-/-}$ mice. The thickness of connecting lines represents the communication likelihood between paired cell clusters, with arrowheads demarcating communication directionality. **d,** Dotplot visualizing signaling of the Spp1 ligand to Cd44 and integrin receptors, denoting interactions between a distinct population of mSCs (mSC-A) and tSCs (tSC-A and tSC-B) in both *S100GFP*-tg (blue) and *S100GFP*-tg *Sod1*$^{-/-}$ (teal) mice. **e**, mRNA levels determined by qPCR for several presumed components of the Spp1 signaling pathway for muscles of *S100GFP*-tg (n = 4) and *S100GFP*-tg *Sod1*$^{-/-}$ (n = 6) mice. **f,g**, Representative immunofluorescent images of NMJs stained with Spp1 (Red), S100B (Green), BTX (White), and DAPI (Blue). Open circles indicate values for individual mice and bars represent the mean across animals ± SEM **P ≤ 0.01, ***P ≤ 0.001, *S100GFP*-tg vs *S100GFP*-tg *Sod1*$^{-/-}$ by two tailed unpaired t-test. Scale bars represent 25 μm.

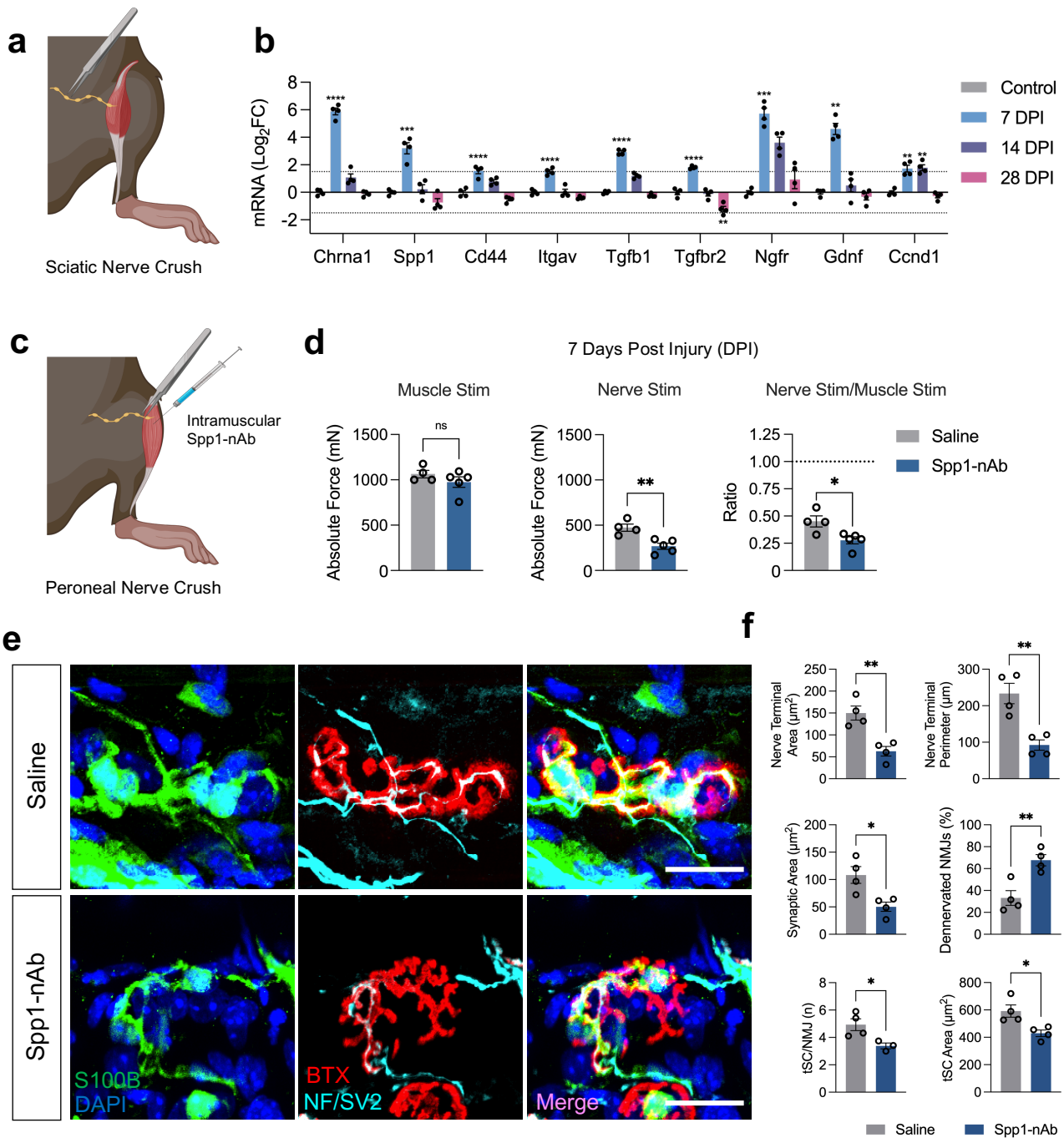
a
Sciatic Nerve Crush
b
mRNA (Log2FC)
Control
7 DPI
14 DPI
28 DPI
Chrna1
Spp1
Cd44
Itgav
Tgfb1
Tgfbr2
Ngfr
Gdnf
Ccnd1
c
Intramuscular
Spp1-nAb
Peroneal Nerve Crush
d
7 Days Post Injury (DPI)
Muscle Stim
Nerve Stim
Nerve Stim/Muscle Stim
Absolute Force (mN)
Ratio
ns
Saline
Spp1-nAb
e
Saline
Spp1-nAb
S100B
DAPI
BTX
NF/SV2
Merge
f
Nerve Terminal Area (μm²)
Nerve Terminal Perimeter (μm)
Synaptic Area (μm²)
Dennervated NMJs (%)
tSC/NMJ (n)
tSC Area (μm²)
Saline
Spp1-nAb

Fig. 6| Spp1 signaling promotes tSC proliferation and muscle fiber reinnervation after nerve injury. a, Sciatic nerve crush injuries were performed, and gastrocnemius (GTN) muscles of C57BL/6 mice were harvested 0 (Control), 7, 14, and 28 days post injury (DPI). **b,** mRNA levels for denervation markers (Chrna1), components of Spp1 signaling (Spp1, Cd44, Itgav, Tgfb1, Tgfbr2), genes associated with SC mediated nerve regeneration (Ngfr, Gdnf), and cell proliferation (Ccnd1) at each time point. **c,** Peroneal nerve injuries were induced and tibialis anterior (TA) muscles were intramuscularly injected with either Spp1-nAb or saline (control) at time of injury and every 2 days thereafter. **d,** Data are shown for force (mN) evoked by direct muscle stimulation, with nerve stimulation, and ratio of force elicited by nerve and direct muscle stimulation at 7 DPI for saline- (gray) and Spp1-nAb-treated (blue) groups. **e,** Representative immunofluorescent images of NMJs at 7 DPI stained with S100B (green), DAPI (Blue), BTX (Red), and NF/SV2 (Cyan). **f,** Quantification of NMJ nerve terminal area and perimeter, synaptic area, percentage of denervated (>10% overlap) NMJs, tSC number and area. Open circles indicate values for individual mice and bars represent the mean across animals ± SEM. Scale bars represent 25 μm. *$P \leq 0.05$, **$P \leq 0.01$, ***$P \leq 0.001$, ****$P \leq 0.0001$ by two tailed unpaired t-test (Saline vs Spp1-nAb) or 1-way ANOVA (7, 14, 28 DPI vs Control) for multiple comparisons.

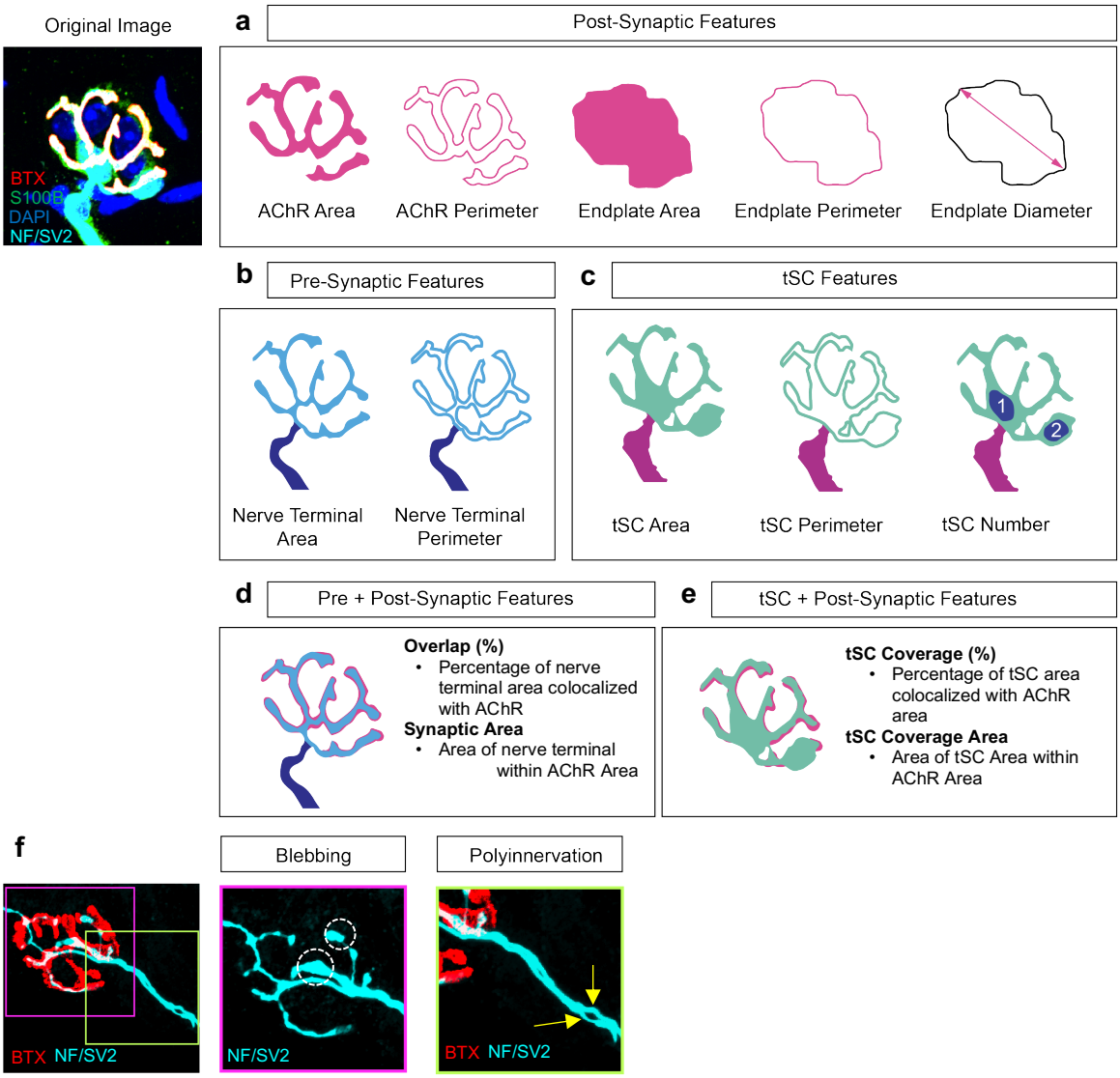

Extended Data Fig. 1| NMJ features analyzed. Binary masks were generated from the original image, and 16 en face NMJ morphological features were measured that represented the **a,** post-synaptic (AChR and Endplate), **b**, pre-synaptic (nerve terminal, axonal blebbing, polyinnervation), and **c**, tSC structures. These pixel measurements are visualized by distinct colorations in each mask: red for post-synaptic features, light blue for pre-synaptic features, and green for tSC structures. **d**, In addition, the percentage "Overlap" between axon terminal and AChR areas were measured. This overlap was further quantified in terms of synaptic area (μm^2), denoting the area where the nerve terminal co-localizes with the AChR region. **e**, Similarly, the "tSC coverage" was determined representing the tSC area that overlaps with the AChR region, and measured the "tSC Coverage Area," which is the expanse of tSC found within the AChR area. **f**, The number of axon terminal blebs and and the presence of polyinnervation were also assessed for each NMJ.

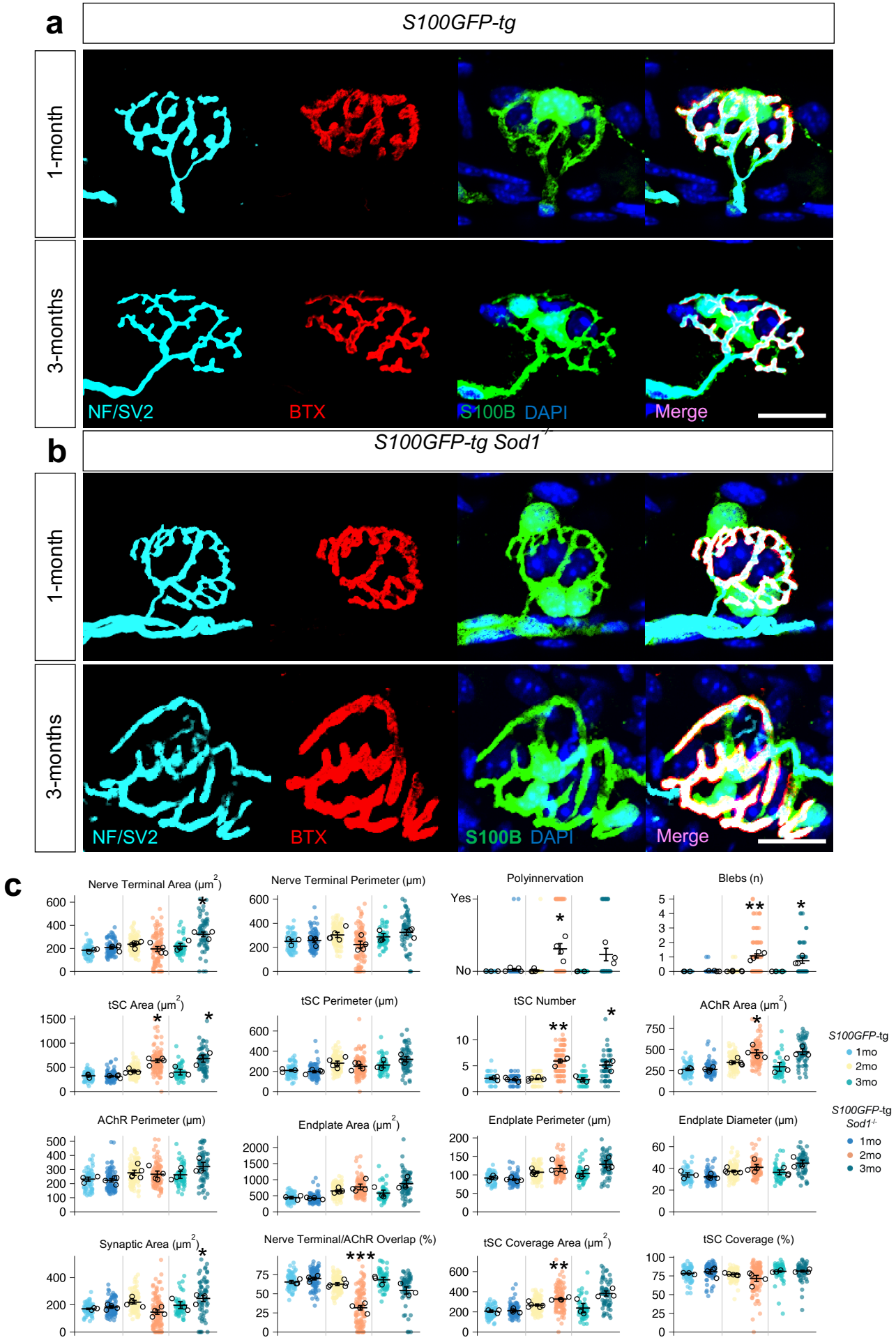
a
S100GFP-tg
1-month
3-months
NF/SV2
BTX
S100B DAPI
Merge
b
S100GFP-tg Sod1-/-
1-month
3-months
NF/SV2
BTX
S100B DAPI
Merge
c
Nerve Terminal Area (μm2)
Nerve Terminal Perimeter (μm)
Polyinnervation
Yes
No
Blebs (n)
tSC Area (μm2)
tSC Perimeter (μm)
tSC Number
AChR Area (μm2)
AChR Perimeter (μm)
Endplate Area (μm2)
Endplate Perimeter (μm)
Endplate Diameter (μm)
Synaptic Area (μm2)
Nerve Terminal/AChR Overlap (%)
tSC Coverage Area (μm2)
tSC Coverage (%)
S100GFP-tg
1mo
2mo
3mo
S100GFP-tg Sod1-/-
1mo
2mo
3mo

Extended Data Fig. 2| Analysis of NMJ in *S100GFP*-tg and *S100GFP*-tg *Sod1*$^{-/-}$ mice. a,**b**, Images of representative NMJs from 1- and 3-month-old mice, stained for S100B (indicating Schwann cells in Green), NF/SV2 (Nerve in Cyan), bungarotoxin (AChR in Red), and DAPI (Nucleus in Blue). **a,** Shows NMJs from S100GFP-tg mice, while **b** are NMJs from *S100*GFP-tg *Sod1*$^{-/-}$ mice. **c,** Graphical representation of NMJ features in *S100GFP*-tg and *S100GFP*-tg *Sod1*$^{-/-}$ mice aged 1, 2, and 3 months. Each colored dot represents a single NMJ. Black circles denote the average for all NMJs in an individual animal. The horizontal bars show the overall mean for each group, while error bars illustrate the mean ± SEM. *Denotes $p < 0.05$ *S100GFP*-tg vs *S100GFP*-tg *Sod1*$^{-/-}$ by two tailed unpaired t-test. Scale bar equals 25 μm and images constrained to the same dimensions.

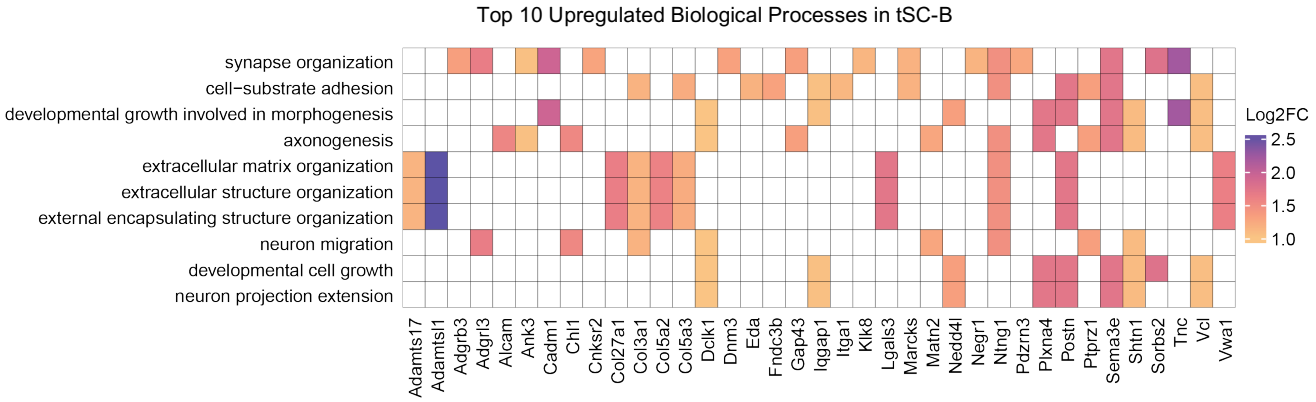

Extended Data Fig. 3| Genes involved in promoting synaptic function and regeneration are upregulated in tSC-B compared to tSC-A and myelin Schwann cells. Heatplot shows the top-10 gene ontology (GO) terms associated with genes upregulated in tSC-B compared to all other muscle-resident Schwann cells identified in this study.

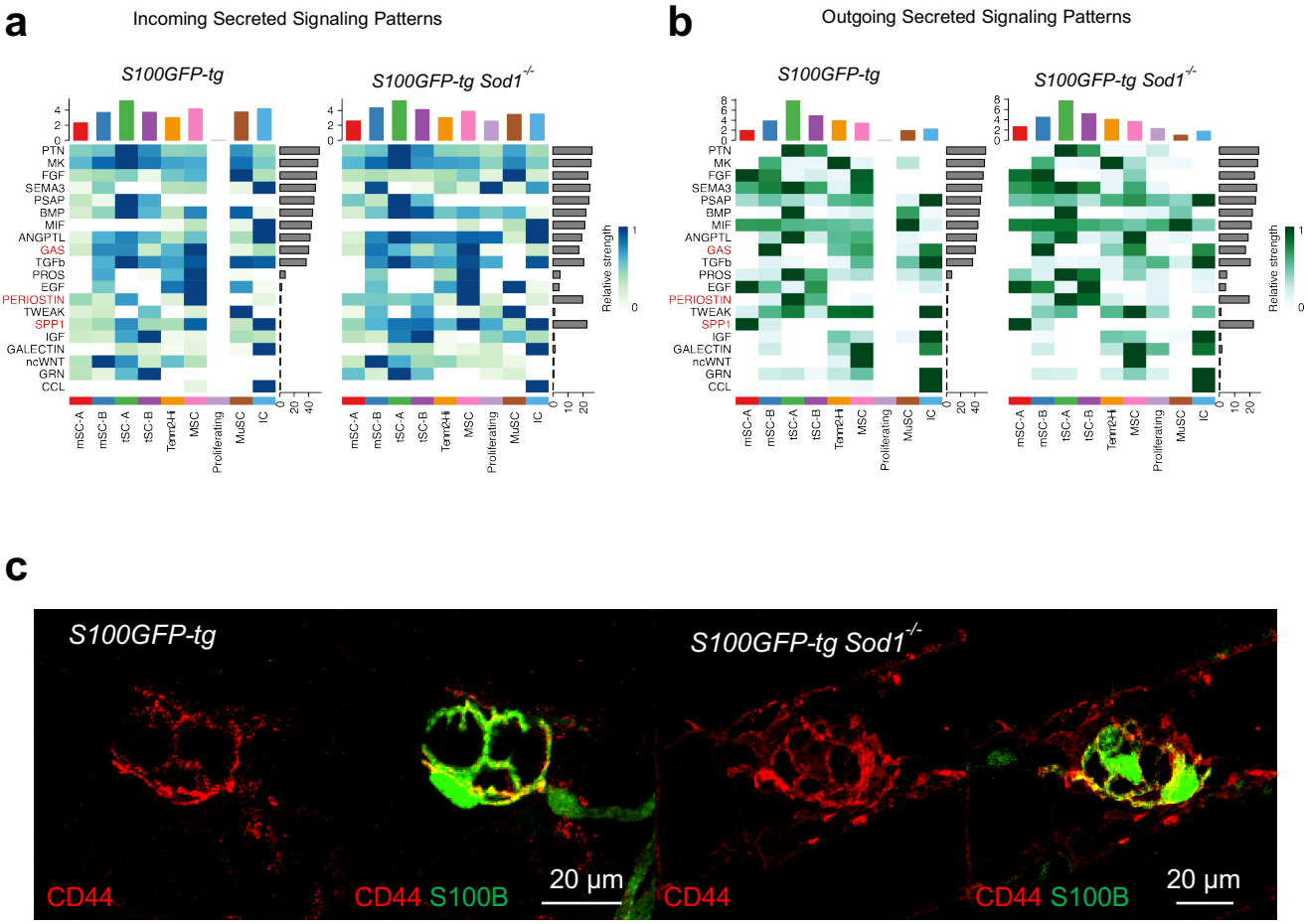

Extended Data Fig. 4| Top 20 intercellular secreted signaling pathways and validation of CD44 protein locatlization. a, Incoming and **b,** outgoing secreted signaling patterns in 2-month-old *S100GFP*-tg *Sod1*$^{-/-}$. Rows delineate distinct signaling pathways, while columns indicate individual cell clusters. Intensity of heatmap color signifies relative signaling strength: darker hues indicate higher signaling strength, and lighter ones suggest weaker signaling. Pathways designated with a red font highlight those most dysregulated in *Sod1*$^{-/-}$ relative to control. mSC, myelin Schwann cells; tSC, terminal Schwann cells; MSC, mesenchymal stem cells; MuSC, muscle stem cells; IC, immune cells. **c,** Representative immunofluorescent images of NMJs stained for CD44 (Red) and S100B (Green).

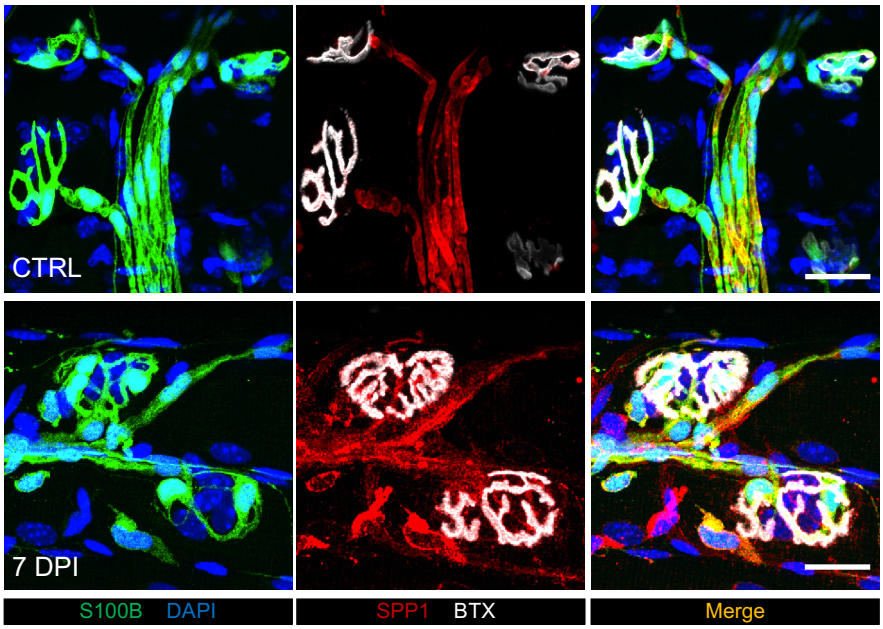

Extended Data Fig. 5| Localization of Spp1 Protein within Skeletal Muscle Fibers. Representative immunofluorescent images of muscle fiber bundles from *S100GFP*-tg mice, captured 7 days post-injury (7 DPI) following sciatic nerve crush, juxtaposed with non-injured controls (CTRL). The staining showcases S100B (Green), SPP1 (Red), BTX (White), and DAPI (Blue). Scale bar represents 25 μm.